Application of the Piecewise Parabolic Method (PPM) to Meteorological Modeling

RICHARD L. CARPENTER, JR.*

Cooperative Institute for Mesoscale Meteorological Studies, Norman, Oklahoma

KELVIN K. DROEGEMEIER

School of Meteorology, University of Oklahoma, Norman, Oklahoma

PAUL R. WOODWARD

School of Physics and Astronomy, University of Minnesota, Minneapolis, Minnesota

CARL E. HANE

National Severe Storms Laboratory, Norman, Oklahoma

(Manuscript received 23 March 1989, in final form 14 September 1989)

ABSTRACT

The Piecewise Parabolic Method (PPM), a numerical technique developed in astrophysics for modeling fluid flows with strong shocks and discontinuities, is adapted for treating sharp gradients in small-scale meteorological flows. PPM differs substantially from conventional gridpoint techniques in three ways. First, PPM is a finite volume scheme, and thus represents physical variables as averages over a grid zone rather than single values at discrete points. Second, a unique, monotonic parabola is fit to the zone average of each dependent variable using information from neighboring zone averages. As shown in a series of one- and two-dimensional linear advection experiments, the use of parabolas provides for extremely accurate advection, particularly of sharp gradients. Furthermore, the monotonicity constraint renders PPM's solutions free from Gibbs oscillations. PPM's third attribute is that each zone boundary is treated as a discontinuity. Using the method of characteristics, the nonlinear flux of quantities between zones is obtained by solving a Riemann problem at each zone boundary in alternating one-dimensional sweeps through the grid. This methodology provides a highly accurate, physically based solution both in the vicinity of sharp gradients and in regions where the flow is smooth.

The ability of PPM to accurately depict the evolution of sharp gradients in small-scale, nonlinear flows is examined by simulating a buoyant thermal and a density current in two dimensions. Comparisons made against gridpoint cloud models reveal that PPM provides superior solutions at equivalent spatial resolution, particularly with regard to resolving shear lines that subsequently become unstable. The PPM model has excellent mass and energy conservation properties, and exhibits virtually no numerical dissipation of resolvable modes. Although PPM is not yet as economical as a conventional gridpoint model, we anticipate that its efficiency can be greatly improved by modifying the treatment of acoustic modes.

1. Introduction

The accurate representation of sharp gradients in meteorological phenomena such as cold fronts, drylines, cloud boundaries, and inversions has long been a challenge for numerical modelers. Conventional gridpoint techniques typically incur large truncation errors near sharp gradients, thereby creating spurious oscillations (the Gibbs phenomenon) which can render the solution physically meaningless. These oscillations may be controlled by using dissipative differencing techniques, such as the first-order upstream scheme, or by imposing artificial viscosity to damp small-scale noise selectively. Unfortunately, both approaches tend to smear gradients in the flow, thus inhibiting adequate representation of potentially important small-scale fluid structures.

With the size and performance of computers increasing at a phenomenal rate, it is tempting to envision that errors associated with sharp gradients in current meteorological models will be reduced to tolerable levels as one employs increasingly higher spatial resolution. Although such an approach may be theoretically valid, it is not likely to be economically feasible or

* Present affiliation: School of Meteorology, University of Oklahoma, Norman, Oklahoma.

Corresponding author address: Dr. Kelvin K. Droegemeier, School of Meteorology, University of Oklahoma, 200 Felgar Street, Room 219, Norman, OK 73019-0470.

computationally practical. For example, a simple doubling of the spatial resolution in a two-dimensional model requires a fourfold increase in computer memory and an eightfold increase in CPU time (in three dimensions the increases are 8 and 16, respectively). All too often the improvement in the solution is too small to justify the expense. In other words, the *convergence rates* of conventional gridpoint techniques are too slow to provide cost-effective improvements in the solution via increases to the spatial resolution alone. Clearly, a *more powerful* numerical approach is called for.

During the past 25 years, many sophisticated techniques have been developed for accurately representing sharp gradients in computational fluid dynamics problems. Most of these advances have occurred in the aerodynamics and astrophysics communities, principally because of the need to accurately represent shock waves, contact discontinuities, and free surfaces. Notable methods include the Marker and Cell (MAC) method (Welch et al. 1965), the Flux Corrected Transport (FCT) method (Boris and Book 1973), the Simple Line Interface Calculation (SLIC) method (Noh and Woodward 1976), the Monotonic Upstream centered Scheme for Conservation Laws (MUSCL) (van Leer 1979; van Leer and Woodward 1979), and the interface tracking method of LeBlanc (see Norman 1980 and the review article by Woodward and Colella 1984). Although quite successful for particular classes of problems, these techniques were formulated for true discontinuities, leaving to speculation their applicability to meteorological flows which exhibit comparatively smooth gradients.

Recent advances in numerical techniques designed specifically for meteorological models can be placed in two categories. In the first are the so-called positive definite schemes, i.e., schemes which do not allow physically positive quantities such as rainwater to become negative (e.g., Smolarkiewicz 1983, 1984; Schneider 1984). Although these methods work quite well and are widely used in the meteorological community, they were not necessarily designed to address problems associated with sharp gradients.

In the second category are adaptive grid techniques, which attempt to provide high spatial resolution locally based on an estimate of the truncation error or on other criteria (Skamarock et al. 1989). A major advantage of some adaptive grid methods is that they are easily applied to an existing numerical framework. As argued previously, however, increasing the spatial resolution either globally or locally may, when coupled with traditional numerical techniques, be insufficient to provide desired accuracy near sharp gradients.

The Piecewise Parabolic Method (PPM) (Colella and Woodward 1984; Woodward 1986), developed originally for modeling astrophysical phenomena such as stellar convection and supersonic jets, represents a drastic departure from finite difference techniques typically used to represent sharp gradients in hydrodynamical problems. (See the review article by Woodward and Colella 1984.) Combining the attributes of several advanced numerical techniques developed over a number of years at the Lawrence Livermore National Laboratory, and containing features of the earlier Godunov (1959) and MUSCL schemes, PPM's strengths are twofold. First of all, it may be classified as a "finite volume" scheme (Rood 1987), i.e., one in which the fluid is represented as a series of *zone-averaged slabs* rather than discrete point values. The zone average is used to construct a *unique parabola* for each dependent variable within a zone (hence, "piecewise parabolic"; see Fig. 1), with the area beneath each curve representing the amount of mass, energy, or other fluid property within the zone. Because each parabola is constrained to be *monotonic,* PPM's solutions are free from numerical oscillations.

It is important to note that, although PPM employs a curve fitting procedure every time step, it has little in common with conventional interpolation methods. For example, spectral methods and splines provide a *global* fit to the data and thus are not well suited for representing localized, sharp transitions. In contrast, the local, zone-by-zone fit afforded by PPM, coupled with its monotonic construction and special steepening procedure in the vicinity of sharp gradients, ensures that positive quantities will remain positive and that sharp gradients will be handled correctly without the generation of spurious oscillations. It is important to note that, because PPM's interpolation procedure is strongly linked to its treatment of hydrodynamical processes (i.e., nonlinear fluxes of quantities between zones), one should not view PPM as simply another interpolation procedure for use in conventional finite difference schemes, but rather as a complete *method* for hydrodynamics.

PPM's second strength arises from the fact that each zone boundary is treated as a (perhaps very small) discontinuity. Pioneered by Godunov (1959) and extended by van Leer (1979), this approach involves constructing a solution to the full hydrodynamical equations by piecing together discontinuous, rather than smooth and continuous, solutions (see also Holt 1984, 28–55). These discontinuous solutions closely approximate the true smooth ones in regions of smooth flow, and are also appropriate for regions where abrupt transitions occur (Woodward and Colella 1984). In applying this concept, Godunov exploited a very simple nonlinear flow problem which has an exact solution: Riemann's shock tube problem. The solution to this problem represents the nonlinear interaction occurring at the discontinuity separating two constant states of a fluid. By representing a fluid numerically as piecewise constant states, each separated by a discontinuity, one can, using the Riemann solution, accurately compute

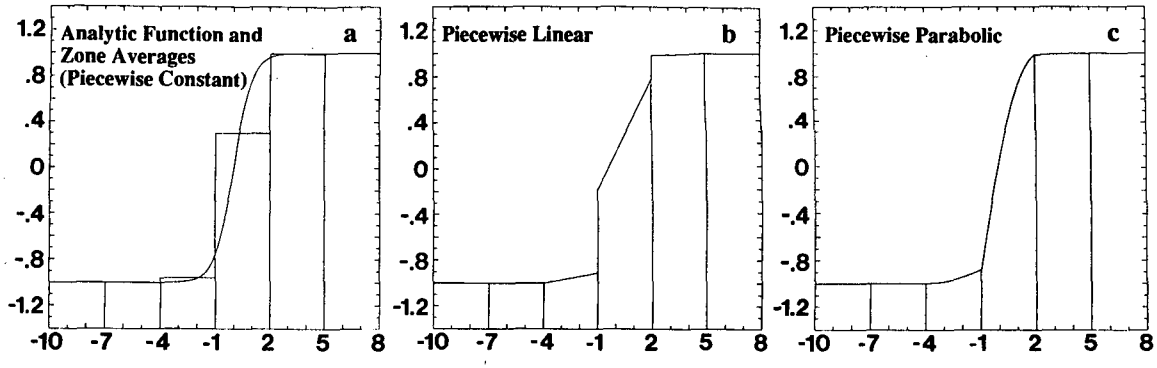

FIG. 1. (a) Piecewise constant, (b) piecewise linear, and (c) piecewise parabolic approximations to a hyperbolic tangent function. In this problem, the domain has been divided into six zones. The analytical function and the associated zone averages (from which the approximations are constructed) are also shown in (a).

the nonlinear flux of quantities between neighboring grid zones. Numerous techniques are now based on Godunov's philosophy [e.g., van Leer (1979); Roe (1981); Harten et al. (1983); Einfeldt (1988); and Parrett and Cullen (1984) and Bennett and Cummins (1988), who used Riemann's problem to solve the shallow water equations], *and perhaps one of the most important aspects of such methods is that an accurate solution is obtained by building into the numerical technique some knowledge of the propagation and nonlinear interaction of waves.*

In section 2 we describe the details of the piecewise parabolic interpolation procedure, and in an attempt to compare PPM with more familiar gridpoint techniques, we present results from linear advection experiments. Section 3 describes the hydrodynamical algorithm, and in section 4 we examine the evolution of a fully turbulent, dry thermal and a density current, and draw comparisons with results from gridpoint cloud models. In section 5, we examine the efficiency of PPM, and summarize our results and present directions for future research in section 6.

2. Interpolation procedure and advection experiments

a. Piecewise parabolic interpolation

In order to understand the philosophy behind PPM, it is important to first recognize the ways in which PPM's representation of dependent variables differs from that of traditional finite difference techniques. While the latter typically describe variables at discrete gridpoints, PPM uses *zone averages,* defined by

$$\langle a \rangle = \frac{1}{\Delta x} \int_{x-\Delta x/2}^{x+\Delta x/2} a \, dx,$$

where a is any variable, such as density, and Δx is the zone width. Figure 1 illustrates this concept by showing how PPM and its predecessors approximate a hyperbolic tangent function. The simplest possible representation is a piecewise constant function (Fig. 1a), which assumes that the dependent variables are distributed uniformly throughout the zone. Godunov (1959) introduced such a representation for hydrodynamical calculations; for advection, this formulation is identical to the familiar first-order upstream scheme. Because the stairstep representation of variables it affords is clearly quite crude, van Leer introduced the monotonic piecewise linear approximation (Fig. 1b) for advection (1977) and hydrodynamics (1979) (cf. the "slopes" scheme of Russell and Lerner 1981). With this approach, neighboring zones are interrogated to estimate the slope of a variable *within* each zone. Note that, in contrast to spectral techniques, which provide a global representation of the dependent variables, this approach provides a local, zone-by-zone representation.

Extending this concept to higher-order interpolation (that is, piecewise parabolic) leads to a much more accurate representation (Fig. 1c). In PPM, a *unique* parabola is constructed within each computational zone using neighboring zone averages. In this manner, the integrated area beneath each parabola (which, for example, may represent the total mass in that zone) is preserved. Care is also taken to maintain the integrity of sharp gradients and to avoid creating new extrema in the distribution (the latter being important for eliminating spurious oscillations near sharp gradients).

An important quality that PPM and its predecessors share is that of *monotonicity.* As stated by van Leer (1977), "The monotonicity condition says that, when a monotonic initial-value distribution is numerically convected, the resulting distribution must be monotonic again." Thus, the monotonicity constraint allows neither the introduction of new extrema nor the amplification of existing extrema during the numerical integration. The result is that sharp interfaces remain free of spurious oscillations and positive quantities remain positive.

We shall sketch here the four steps involved in constructing parabolas on a uniform grid as the process is fully described for both uniform and nonuniform grids by Colella and Woodward (1984). The parabola in any given zone may be uniquely described by the three coefficients (a_0, a_1, a_2) of the following quadratic equation:

$$a(x) = a_0 + a_1 x + a_2 x^2,$$

where x is a normalized zone coordinate. For convenience, however, PPM uses three related parameters: the zone average ($\langle a \rangle$) and the value of the parabola at the left and right zone edges (a_L and a_R, respectively). This leads to a representation given by

$$a(x) = \langle a \rangle + \delta a\, x + a_6 \left(\frac{1}{12} - x^2 \right),$$

where

$$\delta a = a_R - a_L,$$
$$a_6 = 6\langle a \rangle - 3(a_L + a_R)$$

(see Colella and Woodward 1984). When initializing a model using analytical expressions, the zone averages may be obtained exactly. Otherwise, point values may be taken as zone averages. In any event, once the initial zone average is known, construction of parabolas simply involves finding appropriate values for the zone edges.

In the first step of the interpolation process, a piecewise linear distribution (such as that illustrated in Fig. 1b) is constructed. The monotonicity constraint requires that every portion of the distribution in a given zone must lie within the range spanned by the averages in that zone and in its two neighbors. Therefore, the slopes δa are determined by taking the smallest magnitude of three slopes: the centered difference involving both neighboring zone averages, and the two one-sided differences involving each neighbor separately (Fig. 2a). If the zone average itself represents an extremum (Fig. 2b), the slope in that zone is set to zero.

In the second step, "first guess" parabolas (Fig. 3a) are constructed by assigning provisional edge values through the unique cubic curve fit involving the two zone averages and the two slopes surrounding each edge. For example, the left edge in the jth zone has the value

$$a_{L,j} = \frac{1}{2}(\langle a \rangle_{j-1} + \langle a \rangle_j) - \frac{1}{6}(\delta a_j - \delta a_{j-1})$$

(see Colella and Woodward 1984). By using the monotonic slopes described above, this interpolation has the property that the value obtained at a zone edge always lies between the neighboring zone averages. Compared with the analytic solution in Fig. 1a, the first guess interpolation in Fig. 3a weakens the steep gradient and, more importantly, introduces an undershoot and an overshoot in zones 3 and 5, respectively.

In order to determine if a zone contains a discontinuity [which, in the case of astrophysical flows, is necessary for an accurate solution—see Woodward (1986) or Colella and Woodward (1984)], PPM examines the first, second and third derivatives of the density distribution. If a discontinuity exists, the associated parabolas are *steepened* to avoid the smearing of sharp gradients (e.g., those zones marked "S" in Fig. 3b). To ensure that small-amplitude numerical noise is not amplified, relatively tiny jumps (e.g., 1%) in the density, for example, are not steepened.

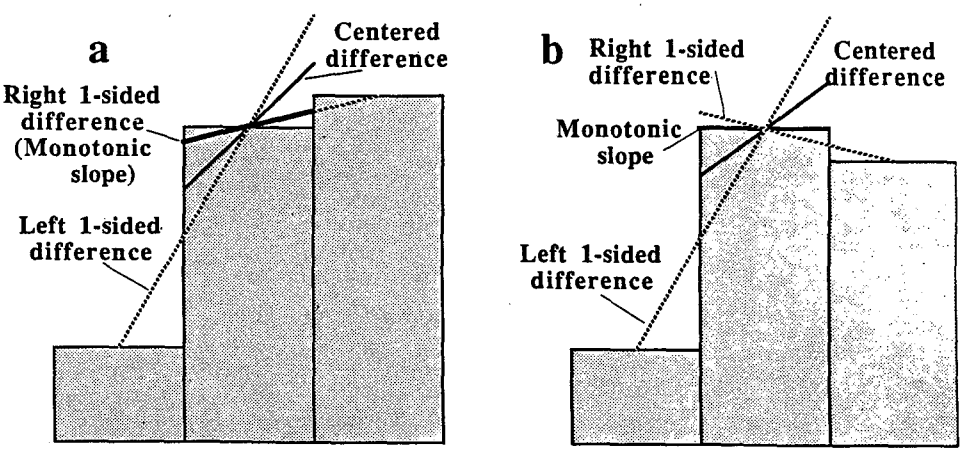

FIG. 2. The construction of a monotonic piecewise linear distribution. (a) The slope in the center zone (bold solid line) is chosen to be the smallest in magnitude of three slopes: the centered-difference approximation (solid line) and the two one-sided approximations (dotted lines). (b) If a zone average represents an extremum, its slope is set to zero.

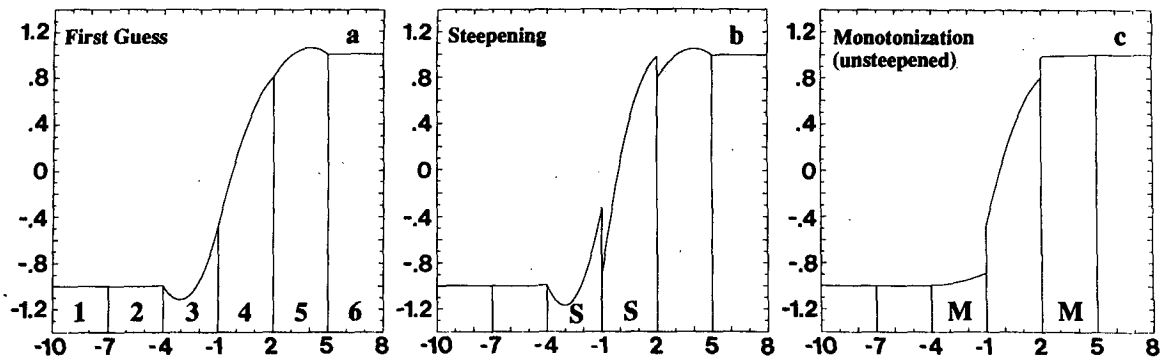

FIG. 3. Steps in creating a piecewise parabolic representation of a hyperbolic tangent function. (The analytic function and associated zone averages are shown in Fig. 1a.) (a) From the zone averages, first guess parabolas are constructed. (b) Parabolas in those zones determined to contain contact discontinuities are then steepened [those zones marked "S" in panel (b)]. (The final, monotonic, distribution is shown in Fig. 1c.) If steepening is not applied, the monotonic distribution in (c) results. Zones marked "M" have been strongly affected by the monotonicity constraint. Adapted from Woodward (1986).

The steepening procedure is computationally expensive because all zones must be tested even if only a few require steepening. Because the meteorological flows considered here contain gradients too weak to exceed the density jump criterion above, and because density varies smoothly in the atmosphere, the steepening routine is in fact never activated in our simulations. (For completeness, the effects of steepening in the context of linear advection are discussed below.)

Finally, the under- and overshoots (zones 3 and 5 in Figs. 3a and 3b) are monotonized (Colella and Woodward 1984), and two cases must be considered in this process. In the first, parabolas are completely flattened if the zone average is a local extremum (similar to the piecewise linear case in Fig. 2b). The second case involves parabolas with amplitudes extending beyond the neighboring zone averages, i.e., those in which $|\delta a| < |a_6|$. In such cases, one of the edge values of the parabola in question is redefined such that the slope of the curve is zero at the opposite edge (Fig. 4). Because both δa and a_6 are known, it is simple to identify which edge value must be changed as well as the degree of change to be applied (see Colella and Woodward 1984, 178–179). The final monotonic, piecewise parabolic distributions without and with steepening are shown in Figs. 3c and 1c, respectively. It is important to note that, throughout the interpolation process, the zone averages never change. Rather, the parabolas are continually adjusted until the final, monotonic distribution is obtained.

It is also important to note that, for *linear* problems, PPM advection yields a solution which is third-order accurate for variable mesh spacing, even if the spacing changes discontinuously (Colella and Woodward 1984). In *nonlinear hydrodynamical* problems such as those discussed in section 4, the directional-splitting technique reduces PPM to second order accuracy. (Note that in the vicinity of sharp gradients, all schemes reduce to first-order accuracy.)

b. Advection experiments

The accuracy of the piecewise parabolic interpolation can be illustrated by solving the one-dimensional linear advection equation

$$\frac{\partial u}{\partial t} + c\frac{\partial u}{\partial x} = 0,$$

where c is the constant and positive advection speed. Figure 5 schematically illustrates the advection procedure in which an analytical function, shown by the solid curve in panel a, is advected toward the right at a Courant number ($\sigma = c\Delta t/\Delta x$) of 0.5. Zone averages

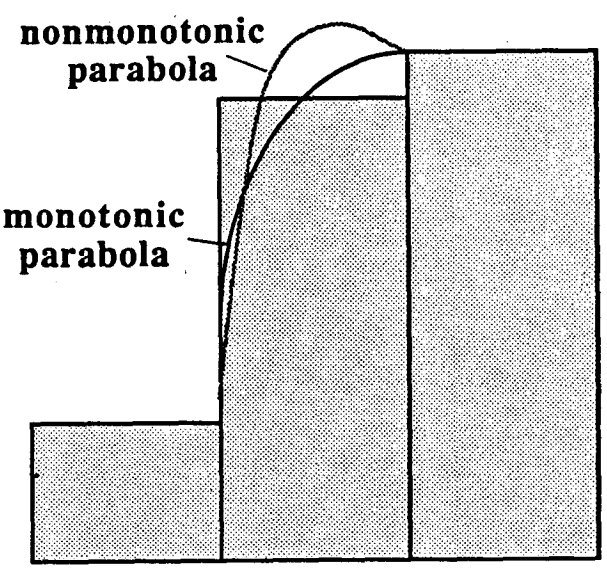

FIG. 4. The monotonization procedure for parabolas. The original parabola in the center zone (stippled line) contains an overshoot. After monotonization, the overshoot has been eliminated while preserving the zone average.

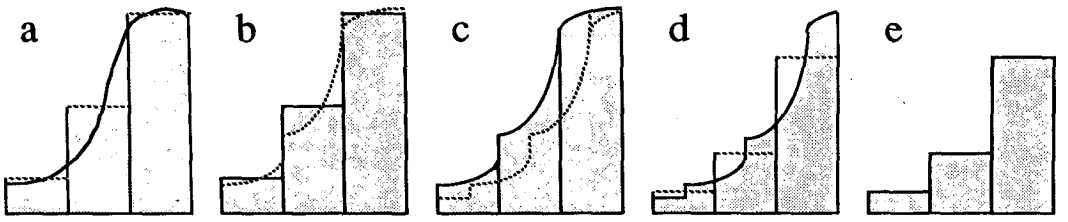

FIG. 5. Schematic illustration of the piecewise parabolic advection procedure. (a) From the initial distribution (solid curve), zone averages (dotted lines) are computed analytically. (This step is performed only at the beginning of the computations.) (b) Using the zone averages (solid lines), a parabola (dotted) is constructed within each zone. (c) The piecewise parabolic distribution is shown before (solid) and after (dotted) advection toward the right at a Courant number of approximately 0.5. (d) After advection, each parabola is integrated analytically to determine the new zone average (dotted). (e) The new zone averages are shown at the end of the time step (the beginning of the next time step). Adapted from van Leer (1977).

(dotted lines in Fig. 5a) are determined by integrating the initial distribution (stippled) over the width of each zone. As described above, a parabola is constructed within each zone (Fig. 5b), and the entire piecewise parabolic representation is exactly shifted toward the right according to $u(x, t + \Delta t) = u(x - \sigma\Delta x, t)$ (Fig. 5c). The portions of the two parabolas lying within a given zone are then integrated analytically to determine the new zone averages (dotted lines in Fig. 5d). These zone averages (Fig. 5e) are then used as initial data for the next time step, and the computation proceeds by determining a new piecewise parabolic representation, as in Fig. 5b. (See also Figs. 1 and 2 in van Leer 1977.)

We now present three cases of 1-D advection and one of 2-D advection in which we compare PPM (with and without steepening) against piecewise constant and piecewise linear advection, and against two examples of finite difference schemes typically used in meteorology: fourth-order centered in space, leapfrog in time and Smolarkiewicz' (1984) positive definite scheme. These comparisons are not meant to be comprehensive or competitive, but rather are intended to illustrate some of the strengths and limitations of PPM.

The first example is the 1-D advection of a rectangular wave one and one-quarter revolutions around a 40-point periodic domain. As shown in Fig. 6a, piecewise constant interpolation (which, as noted above, is identical to the familiar upstream scheme for linear advection) grossly smooths the step function. The fourth-order scheme (Fig. 6b) generates dispersive errors which severely distort the distribution. Smolarkiewicz' scheme (Fig. 6c), with the antidiffusive corrective step applied twice (IORD = 3) also fails to adequately resolve the step. Unlike fourth-order differencing, it broadens the distribution but does not introduce wiggles, i.e., it generates diffusive rather than dispersive errors. (Indeed, it is built upon upstream differencing.) Note that it has amplified the existing maximum, thus demonstrating that a positive definite constraint is less stringent than monotonicity. [A monotonic version of this scheme has now been constructed (Smolarkiewicz and Grabowski 1990).] Piecewise linear advection (Fig. 6d) is both monotonic and free of spurious oscillations and is somewhat less diffusive than Smolarkiewicz's scheme, spreading the gradient over 6 zones. PPM without steepening (Fig. 6e) spreads the gradient over only four zones, and, as a result of monotonicity, exhibits no spurious oscillations. When steepening is applied (Fig. 6f), the gradient is spread over only two zones.

Perhaps a more appropriate test for meteorological applications is the advection of a triangular distribution. Upstream differencing again grossly smooths the distribution (Fig. 7a); however, the fourth-order leapfrog scheme (Fig. 7b) performs quite well. Dispersive waves are still present but are much smaller in amplitude than for the case of the step. The slope of the triangle is well represented, although a small phase error is introduced. Smolarkiewicz' scheme (Fig. 7c) again broadens the distribution somewhat. In particular, note that the first derivative at the base of the triangle is no longer discontinuous. The monotonicity constraint in piecewise linear advection (Fig. 7d) and in PPM without and with steepening (Figs. 7e,f) has clipped the triangle's peak, while PPM's steepener is attempting to change the feature into a square pulse. The transformation of a smooth slope into a step function is a desirable feature when modeling strong shocks on a coarse grid, and is a well-known characteristic of monotonic methods (e.g., Rood 1987). The philosophy is that a feature that cannot be adequately resolved should at least have its position and amplitude properly represented. As demonstrated below, smooth slopes are faithfully represented when they are well resolved. We again note that the steepener is never activated in the meteorological flows presented in this paper.

In the final example of 1-D advection, a Gaussian distribution (with a standard deviation equal to 5% of the domain width) is advected 5 revolutions around an 80-zone periodic grid. This experiment thus provides a demonstration of each schemes' ability to transport well-resolved, smoothly varying functions over large distances. The upstream solution (Fig. 8a) is virtually featureless. Fourth-order leapfrog differ-

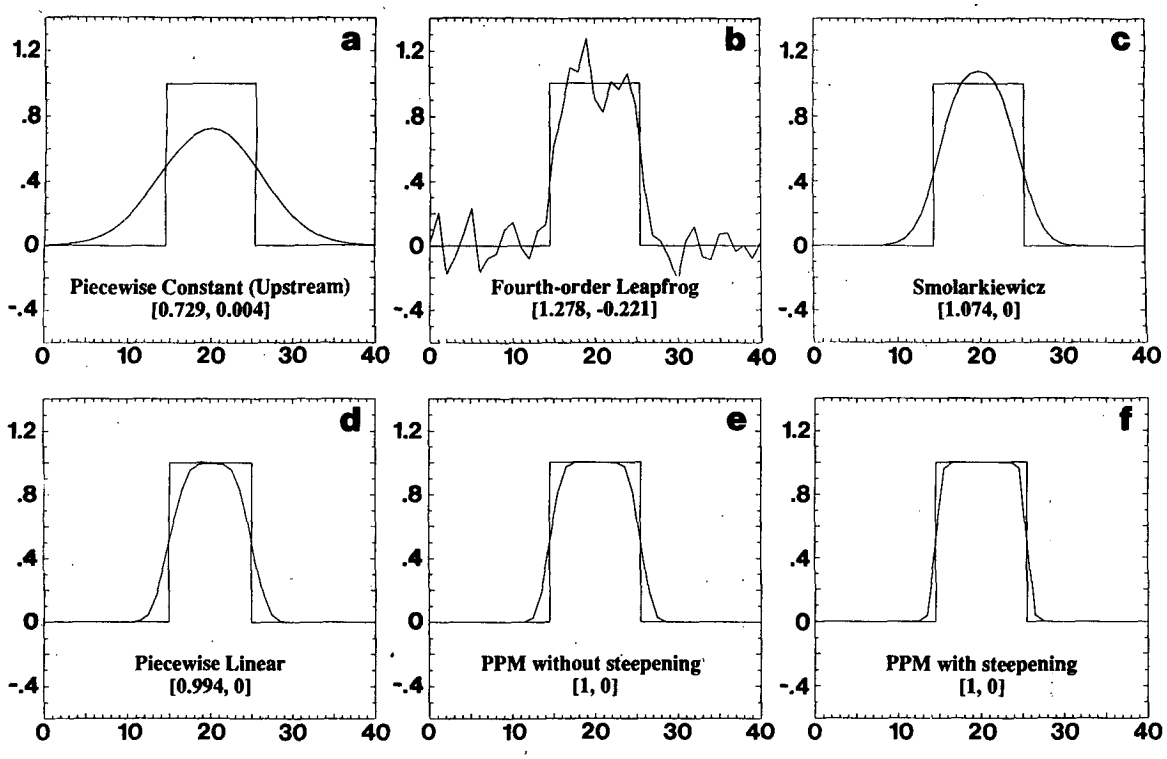

FIG. 6. Solution of the 1-D linear advection equation in which a rectangular wave of unit height is advected toward the right in a 40-point grid with periodic boundaries. The analytical solution is shown after 1.25 revolutions (100 time steps) along with solutions obtained by (a) piecewise constant (upstream) advection, (b) fourth-order centered differencing, (c) Smolarkiewicz' (1984) positive definite scheme, (d) piecewise linear advection, and PPM without (e) and with (f) steepening. Quantities in brackets are maximum and minimum values. (Values smaller than 10^{-7} are presumed to be due to round-off error and have been truncated to zero.)

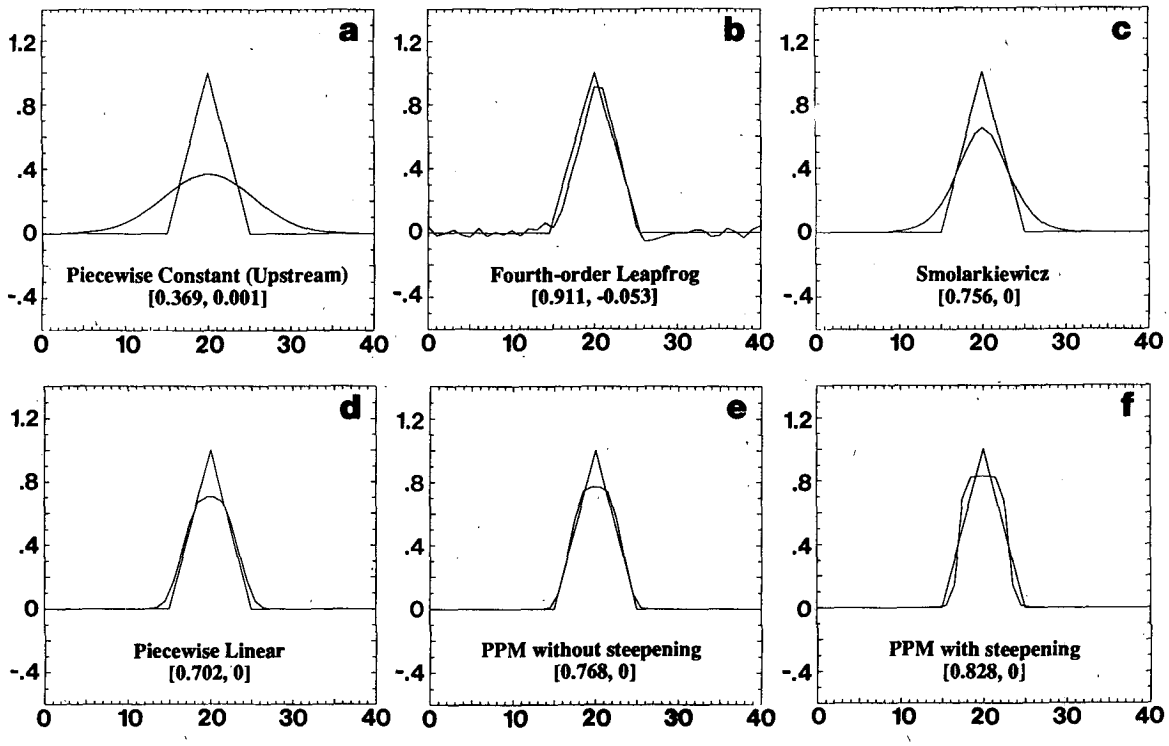

FIG. 7. As in Fig. 6, except for a triangular wave.

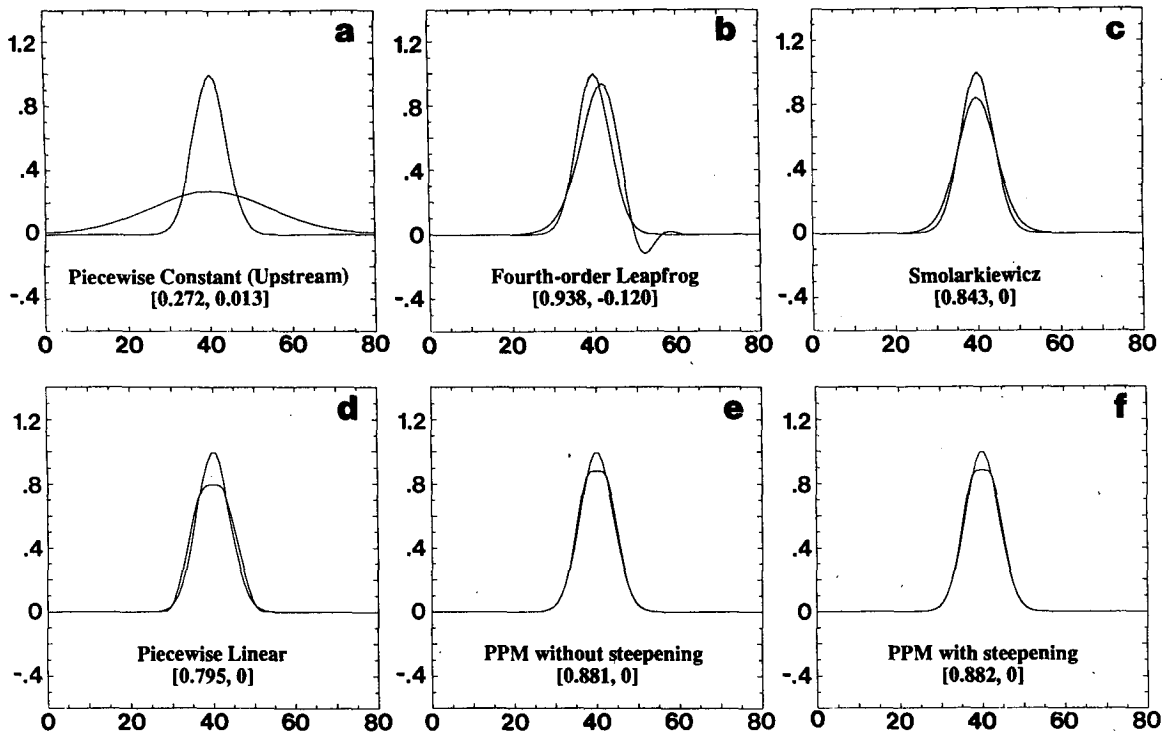

FIG. 8. As in Fig. 6, except for a Gaussian distribution advected 5 revolutions (800 time steps) around an 80-point grid.

encing (Fig. 8b) generates an oscillation downstream from the Gaussian, and exhibits a leading phase error and dispersive damping. The positive definite scheme (Fig. 8c) broadens the distribution somewhat but otherwise advects it quite accurately. Piecewise linear interpolation (Fig. 8d) broadens the distribution while creating a small plateau. Similarly, the unsteepened PPM solution transforms the peak into a plateau about four zones wide as a result of the monotonicity constraint, thus steepening the distribution slightly (Fig. 8e). (Note that the discretized initial conditions represent a plateau two zones wide.) The inclusion of steepening (Fig. 8f) has little effect here because of the smoothness of the function being advected.

Finally, we present results of a 2-D test identical to that reported by Smolarkiewicz (1984), in which a prescribed distribution undergoes solid-body rotation counterclockwise around a 100 × 100 zone grid with open boundaries. The maximum Courant number in the domain is 0.7. The initial condition (Fig. 9a) is the rather severe test proposed by Zalesak (1979): a cylinder of unit height containing a groove five zones wide. The width of the bridge connecting the halves of the cylinder is also five zones.

Upstream differencing results in a grossly smooth, rounded hill of greatly reduced amplitude (Fig. 9b), while the fourth-order leapfrog solution becomes completely unstable after less than one-tenth of a revolution and is not plotted here. Smolarkiewicz' (1984) scheme, formulated in 2-D with cross-terms evaluated and the corrective step applied three times, is shown in Fig. 9c (Fig. 22 from Smolarkiewicz 1984). The groove and bridge are both evident though somewhat eroded, and an empirical switch, which turns off the corrective step in the vicinity of shocks, has preserved some of the plateau (rather than forming a peak of increased amplitude).

Piecewise linear interpolation (Fig. 9d) resembles the Smolarkiewicz solution, although the groove is somewhat more eroded and the sides are steeper. PPM without steepening (Fig. 9e) erodes the groove and bridge by nearly the same amount as the Smolarkiewicz scheme, although the plateau is better represented and the sides are much steeper. The PPM solution with steepening (Fig. 9f) very closely resembles the initial conditions; the edges are rounded slightly, leaving the bridge and groove perhaps three zones wide. Quite remarkably, the amplitude of the function remains unity across the bridge and zero in the groove.

To conclude our discussion of linear advection, two points are worth noting. First, although we have demonstrated that PPM performs quite well on linear advection problems, we have not attempted to show that it is the most *economical* technique available (this issue is addressed in section 5). Second, linear advection is but one of many processes represented in a numerical model, and the more interesting case of fully nonlinear flow is considered below.

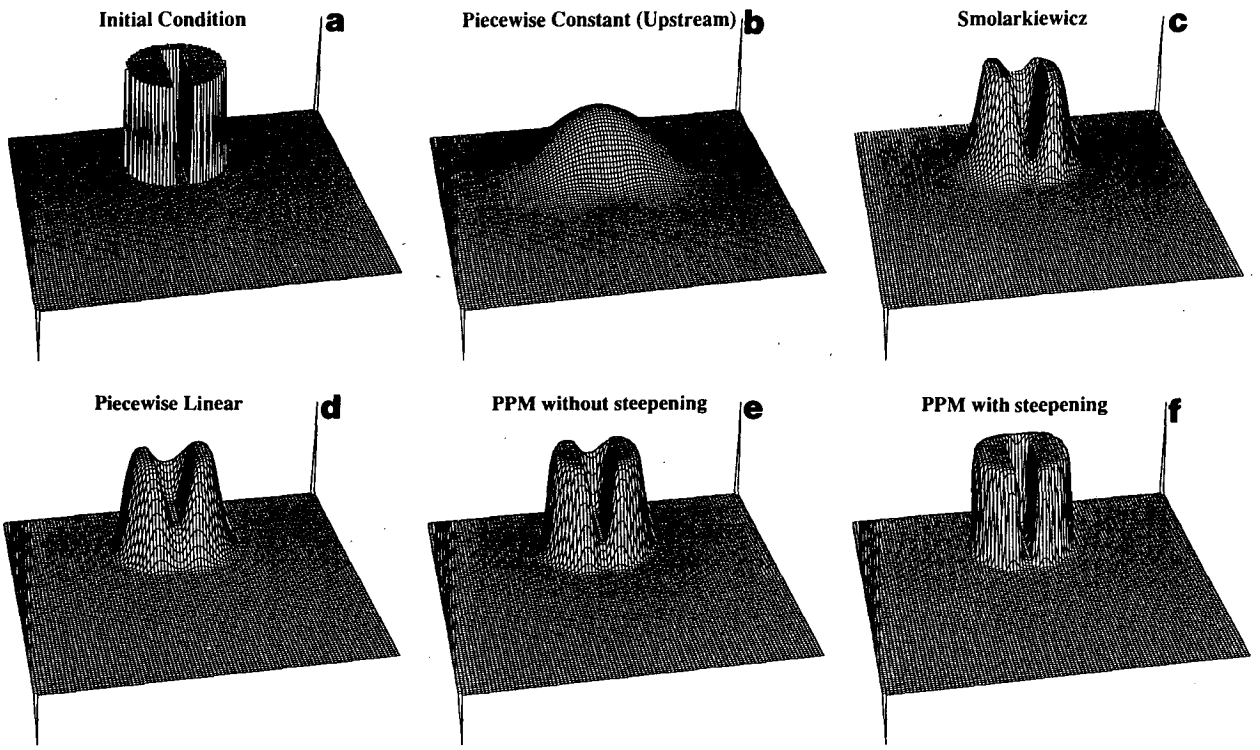

FIG. 9. Solution of the 2-D linear advection equation in which a grooved cylinder of unit height undergoes solid-body rotation counterclockwise one revolution in a 100 × 100 grid with open boundaries. (a) Initial condition, (b) piecewise constant (upstream) differencing, (c) Smolarkiewicz' (1984) positive definite scheme [Fig. 22 from Smolarkiewicz (1984)], (d) piecewise linear differencing, (e) PPM without steepening, (f) PPM with steepening. The maximum Courant number is 0.7. The spikes in the foreground and background are −0.5 and 1 unit high, respectively.

3. Hydrodynamics

We now use the advection algorithm described in section 2 as a basis for solving the complete set of nonlinear hydrodynamical equations in Lagrangian mass coordinates. This process involves four steps (see Colella and Woodward 1984, 181): 1) parabolas are interpolated within each zone for all dependent variables; 2) the governing equations in characteristic form comprise a Riemann problem which is solved at each zone boundary; 3) the Riemann solutions are used to compute nonlinear spatial fluxes which are differenced conservatively; and 4) parabolas are again interpolated and all variables are remapped conservatively from the nonuniform Lagrangian mesh to a uniform Eulerian mesh.

a. Governing equations

The equations describing the time evolution of mass, momentum per unit mass, and thermodynamic energy per unit mass (written in terms of pressure) for a dry, inviscid, compressible and isentropic fluid in a nonrotating reference frame are:

$$\frac{D\rho}{Dt} = -\rho\nabla\cdot\mathbf{V} \tag{1}$$

$$\frac{D\mathbf{V}}{Dt} = -\frac{1}{\rho}\nabla p - g\mathbf{k} \tag{2}$$

$$\frac{Dp}{Dt} = -c^2\rho\nabla\cdot\mathbf{V}, \tag{3}$$

where c is the Eulerian sound speed ($c^2 = \gamma RT$, where $\gamma = c_p/c_v$; R is the gas constant for dry air, and c_p and c_v are the specific heats at constant pressure and volume, respectively). ρ is the dry air density, $\mathbf{V}$ is the velocity vector, p is the pressure, g ($=9.8\ \mathrm{m\ s^{-2}}$) is the gravitational acceleration directed opposite to the local vertical coordinate (unit vector $\mathbf{k}$), and D/Dt denotes a substantial derivative.

As a result of compressibility, this set of equations admits acoustic wave modes which, for meteorological models, serve only as a nuisance by imposing a severe restriction on the time step. Nevertheless, given the complexity of the astrophysical version of PPM and our initial unfamiliarity with several associated concepts (e.g., Riemann's problem), we chose to first develop a compressible version of the code appropriate for nonshocked (meteorological) flows, and then proceed to improve the model's efficiency through changes to the solution process (e.g., the mode-splitting technique of Klemp and Wilhelmson 1978). This paper

presents results of the former effort, while the latter is currently being undertaken (see sections 4 to 6).

We now proceed to write the governing equations in a form appropriate for PPM. First, it is convenient to use Cartesian coordinates and a uniform grid. [Cylindrical and spherical coordinate systems, as well as nonuniform grids, are discussed in Colella and Woodward (1984).] Second, for physical relevance, we employ mass, rather than distance, as an independent variable and solve the conservation laws in Lagrangian form. (In order to avoid severe grid distortions that might occur in a fully turbulent fluid, we remap all variables back onto the reference Eulerian grid after each Lagrangian time step.) Third, because of the intractability of solving Riemann's problem in more than one dimension, PPM is formulated as a one-dimensional scheme and is easily extended to two or three dimensions through the well-known technique of directional-splitting (Strang 1968). In this technique, a multidimensional problem is solved via successive, one-dimensional sweeps in each of the coordinate directions. Finally, because thermodynamic variables in the atmosphere vary more rapidly in the vertical than in the horizontal, we write them as the sum of a basic state which varies only with height (denoted by a zero subscript) and a deviation (denoted by a prime), which need not be small, i.e.,

$$\xi(x, y, z, t) = \xi_0(z) + \xi'(x, y, z, t).$$

We then subtract from the momentum and pressure equations the hydrostatically balanced base state ($dp_0/dz = -\rho_0 g$).

The resulting one-dimensional nonlinear equations written in Lagrangian (mass) coordinates are

$$\frac{\partial \rho}{\partial t} = -\rho^2 \frac{\partial u}{\partial m} \tag{4}$$

$$\frac{\partial u}{\partial t} = -\frac{\partial p'}{\partial m} - \frac{\rho' g}{\rho} \tag{5}$$

$$\frac{\partial p'}{\partial t} = -C^2 \frac{\partial u}{\partial m} + \rho_0 g u. \tag{6}$$

Here, m is the mass coordinate (where $\Delta m = \rho \Delta x$, and both m and x are taken to be in the direction of the sweep), u is the longitudinal (that is, in the direction of the sweep) velocity defined by

$$\frac{\partial x}{\partial t} = u, \tag{7}$$

and C ($=\rho c$) is the Lagrangian sound speed. Terms involving gravity are, of course, zero during horizontal sweeps. We have replaced total derivatives with partial derivatives because the advection terms have vanished in the Lagrangian framework. Note also that we have *not* employed the binomial approximation in writing the buoyancy term in Eq. (5).

In order to improve accuracy, we replace the pressure Eq. (6), which is merely a statement of the first law of thermodynamics, by an explicit statement of conservation of entropy

$$\frac{\partial}{\partial t} \frac{p}{\rho^\gamma} = 0, \tag{8}$$

and write the mass continuity equation in conservation form

$$\frac{\partial}{\partial t} \frac{1}{\rho} = \frac{\partial u}{\partial m}. \tag{9}$$

The conservation equations used by PPM are therefore (5), (8), and (9), along with a description of fluid element locations (7).

b. *Lagrangian hydrodynamics*

After the initial conditions have been specified and the parabolas constructed, the governing equations are integrated forward in time for each computational zone. Because PPM is a "finite volume" technique and is based on zone-averaged data, the equations are also integrated over the area of the zone. For the momentum equation (5), the integration in time from t to $t + \Delta t$ and in space (mass) from m to $m + \Delta m$ may be written as

$$\int\int \frac{\partial u}{\partial t}\, dt\, dm = -\int\int \frac{\partial p'}{\partial m}\, dm\, dt - g \int\int \frac{\rho'}{\rho}\, dt\, dm \tag{10}$$

and evaluated as

$$\langle u \rangle_{new} = \langle u \rangle - \frac{\Delta t}{\Delta m} (\overline{p}'_R - \overline{p}'_L) - \overline{\left\langle \frac{\rho'}{\rho} \right\rangle} g \Delta t, \tag{11}$$

where $\langle\ \rangle$ denotes zone averages at the beginning of the time step, $\langle\ \rangle_{new}$ denotes zone averages at the end of the Lagrangian time step [but before remapping (see section 3c)], L and R denote the left and right edges of the associated computational zone, and an overbar denotes a temporal average, given by

$$\overline{(\ )} = \frac{1}{\Delta t} \int_t^{t+\Delta t} (\ )\, dt.$$

Thus, in order to compute the new average momentum in a zone (Fig. 10), we must know the average momentum at the beginning of the time step, the time-averaged pressure along both edges of the zone, and the time- and space-averaged buoyancy. Note that, when updating one of the momentum components in a sweep during the Lagrangian calculations, the other component is held fixed. The consequences of this approximation are discussed in section 4a.

Integrating the equations for zone location (7), mass (9), and the adiabatic constant (8), we have for each zone

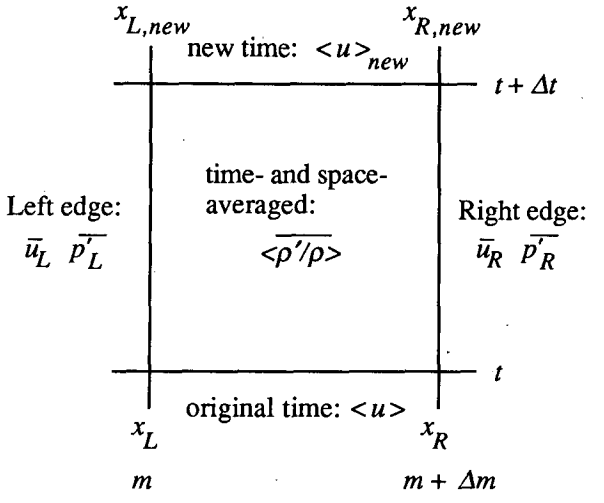

FIG. 10. Space–time diagram showing the location of variables involved in updating the momentum equation (11). See the text for further details.

$$x_{L,\,new} = x_L + \bar{u}_L \Delta t \tag{12}$$

$$\left\langle \frac{1}{\rho} \right\rangle_{new} = \left\langle \frac{1}{\rho} \right\rangle + \frac{\Delta t}{\Delta m} (\bar{u}_R - \bar{u}_L) \tag{13}$$

$$\left\langle \frac{p}{\rho^\gamma} \right\rangle_{new} = \left\langle \frac{p}{\rho^\gamma} \right\rangle, \tag{14}$$

where x_L is the location of the left zone edge and $\bar{u}_L$ ($\bar{u}_R$) represents the time-averaged velocity at the left (right) zone edge. Equations (11)–(14) compose the system to be integrated each time step. Given the *location* of each zone edge (x), the *zone averages* of mass, momentum, and pressure ($\langle \rho \rangle$, $\langle u \rangle$, $\langle p \rangle$), the *time-averaged fluxes* of momentum ($\bar{u}_{R,L}$) and pressure ($\bar{p}_{R,L}$) at the zone edges, and the *time- and space-averaged buoyancy,* we can then solve for zone averages at the new time level.

Everything needed to solve the system is known except for the time-averaged fluxes and the time- and space-averaged buoyancy. The fluxes are obtained using the *method of characteristics.* In this technique certain quantities, called *Riemann invariants,* are conserved along the characteristic paths of sound waves (e.g., Courant and Friedrichs 1948; Holt 1984, 6–8; Anderson et al. 1984). On a space–time diagram, sound waves impinging on a zone edge form two distinct *domains of dependence* (Fig. 11), and Riemann's problem involves solving for the nonlinear interactions along the vertical line separating these two domains of dependence (which are represented as constant states of the fluid).

The *characteristic equations* describing sound waves trajectories,

$$dm = \pm C\, dt, \tag{15}$$

and the *compatibility equations* describing the quantities conserved along these characteristics,

$$du \pm \frac{dp'}{C} = \left(\frac{-\rho' g}{\rho} \pm \frac{1}{C} \rho_0 g u \right) dt, \tag{16}$$

are derived in the Appendix. Here, du is the change in momentum, defined as $\bar{u} - \langle u \rangle_+$, or $\bar{u} - \langle u \rangle_-$, depending on which characteristic equation [right-moving waves (+) or left-moving waves (−)] is chosen, and dp' follows similarly. Also, $\bar{u}$ is the time-averaged momentum along the zone edge separating the two domains of dependence, $\langle u \rangle_+$ is the spatially averaged momentum in the left domain of dependence (corresponding to the rightward propagating characteristic), and $\langle u \rangle_-$ is the spatially averaged momentum in the right domain of dependence (corresponding to the leftward propagating characteristic). A simple interpretation of (16) is that, in the absence of gravity, and assuming that C is constant within the domain of dependence, the quantity $u + p'/C$ ($u - p'/C$) is conserved along right-moving (left-moving) sound waves.

We should emphasize that, because shock waves are absent in the subsonic meteorological flows considered here, our Riemann solver is much simpler than that used in the astrophysical version of PPM. Further, the original version of PPM had no buoyancy term on the right-hand side of (16), but instead had source terms arising from body forces or nonplanar symmetry which were incorporated into "effective" momenta and pressures in Riemann's problem (Colella and Woodward 1984).

The solution of Eq. (16) proceeds as follows. After computing a Courant number (that is, the width of the domain of dependence) in each zone based on the average Lagrangian sound speed within that zone $\langle C \rangle$, we interpolate parabolas for u, p', and ρ' and integrate them over the left and right domains of dependence

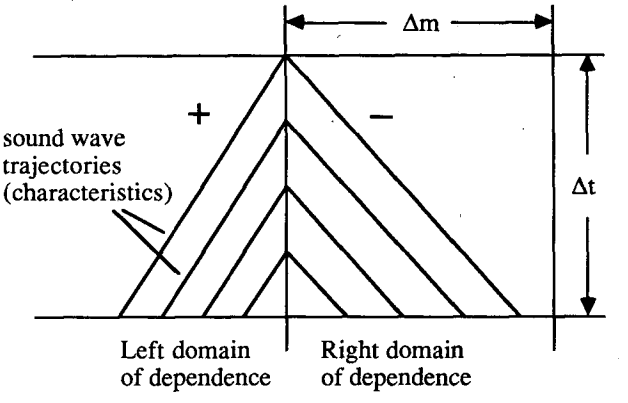

FIG. 11. Schematic representation of the solution domain for Riemann's problem. The slanted lines depict the characteristic curves of sound waves traveling toward the right (+) and left (−) in the left and right domains of dependence, respectively. The slope of the characteristics represents the local sound speed.

for each zone edge to find *domain averages* (similar to zone averages). We then use $\langle C \rangle$ in solving Riemann's problem for $\bar{u}$ and $\bar{p}'$ at each zone edge [Eqs. (16)]. We may immediately use $\bar{u}$ to compute the new zone edge locations (x_{new}) [Eq. (12)].

We then use the new zone edge locations to compute the new density in each zone. The calculation handles the base state and perturbation density separately so as to retain the accuracy of the perturbation form. Base state density does not change (following a parcel) when a parcel moves horizontally, but does change for vertical displacements. Thus, during vertical sweeps the new zone-averaged base state density is computed in a manner analogous to remapping (section 3c).

Because mass is conserved following a parcel, we may compute the new perturbation density as

$$\langle \rho' \rangle_{new} = \frac{\langle \rho' \rangle \Delta x - \langle \rho_0 \rangle_{new} \Delta x_{new} - \langle \rho_0 \rangle \Delta x}{\Delta x_{new}},$$

where Δx and Δx_{new} are the zone widths before and after the Lagrangian step, respectively. During vertical sweeps, the quantity in parentheses is simply the mass which was added to the zone as a result of the changing base state density; during horizontal sweeps this quantity may be expressed as $\langle \rho_0 \rangle \Delta t (\bar{u}_R - \bar{u}_L)$.

Finally, the time- and space-averaged buoyancy in the vertical momentum equation (11) is evaluated as

$$\overline{\left\langle \frac{\rho'}{\rho} \right\rangle} \approx \frac{\overline{\langle \rho' \rangle}}{\overline{\langle \rho \rangle}},$$

where the numerator and denominator on the right-hand side are each approximated as half the sum of the old and new zone averages. The adiabatic constant (14) and the momentum component transverse to the direction of the sweep are unchanged during the hydrodynamics step.

c. Eulerian remap

At this point all "new" quantities are known in the Lagrangian frame of reference following a fluid parcel. According to (12), the positions of the zone edges move during the Lagrangian step, and thus to avoid potentially severe distortions in the grid we map all quantities in the nonuniform Lagrangian grid to the original, uniform Eulerian grid after each time step. Because the zone averages are already known, this simply amounts to redefining the locations of the zone edges and creating new parabolas. PPM's high-order interpolation procedure during the remap avoids the smearing typically associated with Eulerian differencing techniques, and is in fact analogous to pure linear advection (see Fig. 5).

Using the volume coordinate (x), the perturbation and basic state densities are the first variables to be interpolated and remapped. The remaining variables (adiabatic constant and momentum, including the momentum component transverse to the direction of the sweep which was passively advected during the hydrodynamics step) are then interpolated and remapped using mass as the independent variable.

d. Boundary conditions

Boundary conditions are implemented by constructing three artificial zones beyond the physical boundaries of the domain (Fig. 12). (*Three* zones are needed in order to construct parabolas in the artificial zone nearest the boundary.) We employ rigid boundaries in the thermal simulations in section 4 in order to easily compare PPM's conservation properties to those of other schemes and to the known properties of the physical system. In this case, we supply the artificial zones with mirror images of the zone averages nearest the boundary, and reverse the sign of the longitudinal momentum component (Fig. 12a).

Because of PPM's strict monotonicity constraint, spurious waves are never generated at the boundaries. An unfortunate consequence of this constraint, however, is that variables on either side of a boundary, except for the longitudinal momentum, have the same

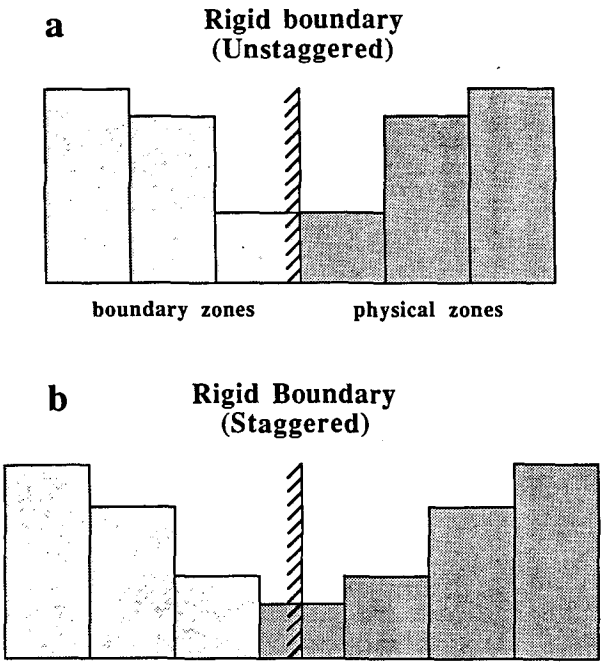

FIG. 12. Implementation of rigid boundary conditions. Heavy (light) stippling denotes physical (boundary) zones, and the hatched line denotes the physical boundary. (a) In the general case ("unstaggered" rigid boundary), the boundary zones are mirror images of the physical zones (except for the velocity component normal to the boundary, whose sign is reversed). Unfortunately, this leads to completely flattened parabolas in the zones immediately on either side of the boundary. (b) By allowing the boundary to lie in the middle of the first physical zone ("staggered" rigid boundary), parabolas need be flattened only in a single zone. The width of the boundary influence is therefore halved.

value, thus producing a local extremum *at* the boundary (for reasons cited below, we call this the "unstaggered" rigid boundary). The monotonicity constraint requires that the parabolas in the zones immediately on either side of the boundary be completely flattened, thereby reducing the method to piecewise constant at the boundary (locally first order). This effect may be reduced from one zone in width to one-half zone in width by simply adding an extra zone (Fig. 12b). In this case the physical boundary lies in the middle of the zone (which we refer to as a "staggered" rigid boundary), and only the parabola in this zone will be flattened. As discussed in section 4, this change has a clear impact on the numerical solution for certain types of problems.

Open boundaries, which allow flow to be directed into or out of the domain, have also been constructed and will be demonstrated for gravity current simulations in section 4. If the average velocity in the zone nearest the boundary is directed out of the domain (outflow condition), the artificial boundary zones take on the values of the variables in the physical zone nearest the boundary. Conversely, if the normal velocity at the boundary is directed into the domain (inflow condition), the boundary zones are supplied with values of the known base state.

4. Meteorological simulations

In order to establish PPM's ability to model meteorological processes, we simulate the evolution of two phenomena characterized by sharp gradients: a buoyant thermal and a density current, each using a dry and neutrally stable (isentropic) atmosphere in a slab-symmetric framework.

The laboratory counterpart of the thermal experiment received much attention several years ago (e.g., Scorer 1957, 1958; Woodward 1959; Richards 1961), and was critical for verifying the self-similar nature of convective plumes (e.g., Batchelor 1954; Morton 1957; Squires and Turner 1962). Early efforts directed toward numerically modeling buoyant thermals in two dimensions were plagued by nonlinear instabilities (Ogura 1962) and by limited computer resources (Lilly 1962). By using a coordinate system which expanded with time, Lilly (1964) overcame the latter constraint and studied the nonlinear dynamics of the evolving flow field. Owing in part to the significant differences between two- and three-dimensional turbulence (e.g., Lilly 1969; Tennekes 1978), however, none of these works completely reproduced the expectations of similarity theory. Fox (1972) extended Lilly's (1964) study to three dimensions, and found good agreement between his numerical results and similarity theory for laminar flow. Unfortunately, he was unable to simulate flows with Reynolds numbers greater than about 50. Since that time, investigators have continued to study the dynamics of buoyant thermals (see the review by Pearson 1980), with only the most recent simulations showing promise of explicitly representing sharp gradients and turbulent entrainment through the use of high spatial resolution (Klaassen and Clark 1985).

The present work focuses on the explicit representation of turbulent processes in buoyant thermals, particularly shearing instabilities, which depend upon an accurate treatment of scalar and momentum gradients. Two sets of experiments, differing primarily in domain size, are described in sections 4a, b. Simulation results from the PPM code are compared to solutions obtained using the two-dimensional cloud model developed by Droegemeier and Wilhelmson (1987) (hereafter referred to as DW). Both models are run at various resolutions to illustrate relative performance in accuracy and economy, with the accuracy of the PPM interpolation algorithm evaluated by comparative simulations using piecewise linear and piecewise constant interpolation.

Because buoyant thermals are highly turbulent entities whose *detailed structure* is perhaps rather sensitive to model formulation, it was believed that a somewhat less violent flow would prove instructive in evaluating PPM's capabilities. Therefore, in section 4c, we simulate a density current and compare our results with those from the 2-D adaptive-grid cloud model of Skamarock and Klemp (1989).

a. Small domain thermal experiments

In this set of experiments, convection is initiated by placing a warm thermal perturbation 1 km above the lower boundary in a domain 4 km high and 3.2 km wide (Fig. 13). The bubble has a radius of 1 km and a potential temperature excess of 2 K at its center which decreases smoothly to 0 K at its edge. The environment has a constant potential temperature of 300 K, and we exploit the symmetry of the problem to reduce computational expense by modeling only the right half of the total physical domain.

1) CONTROL EXPERIMENT

We designate the control experiment PPM-20S (see Table 1), where the prefix denotes the model (PPM) and the suffix denotes the spatial resolution (here 20 m) and the relative domain size (S for small domain). "Staggered" rigid boundaries (section 3d) are employed on all sides of the computational domain, which is 81 zones high by 201 zones wide.

The evolution of the thermal is described in a series of contour plots of the perturbation potential temperature θ', which is proportional to the thermal buoyancy, and the vertical velocity w (Figs. 14a–f). The maximum in thermal buoyancy is located on the symmetry axis, and thus the center of the thermal rises the fastest. The buoyancy gradient atop the thermal steepens rapidly due to nonlinear effects (Fig. 14b), with the maximum

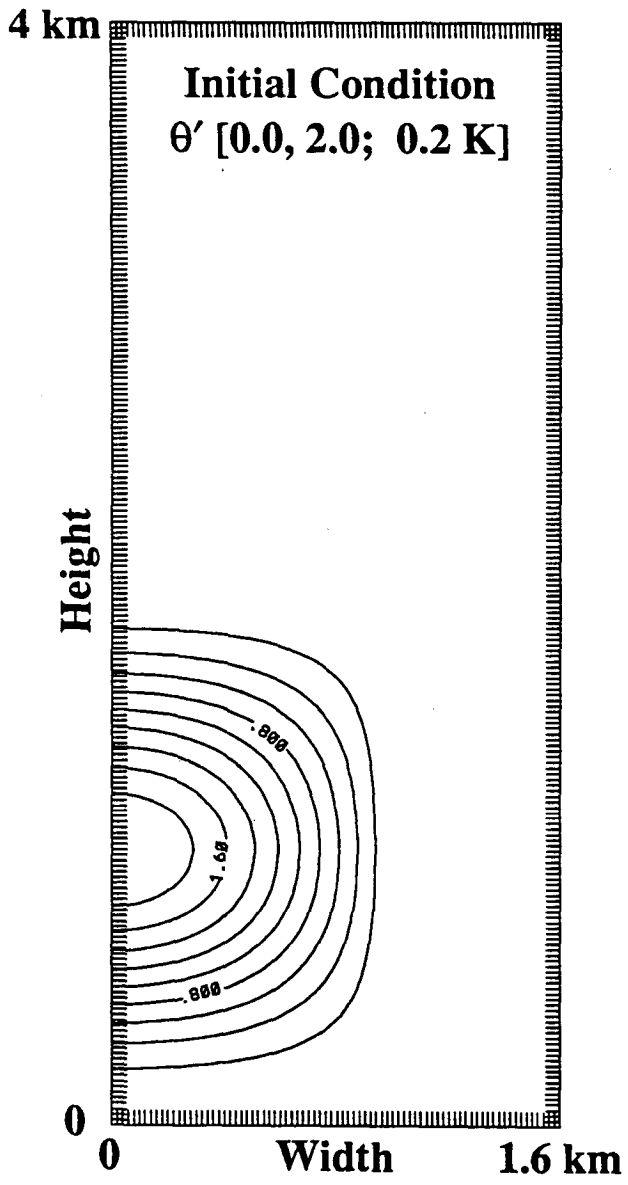

FIG. 13. Initial perturbation potential temperature field (θ', deg K) for the small domain thermal simulation experiments. For this and all subsequent thermal figures, the square brackets indicate [minimum value, maximum value; contour interval], and the zero contour is not plotted in the perturbation potential temperature fields.

vertical velocity (7.6 m s^{-1} at 8 min—see Fig. 15) also occurring along the axis of symmetry. The thermal begins to decelerate as it nears the (rigid) upper boundary, and by 10 min (Fig. 14b) the right side of the thermal begins to plunge downward in response to a strong vortical circulation which is accentuated by the relatively small domain size. This vortical circulation causes the potential temperature maximum to migrate laterally away from the symmetry axis, a feature noted in other numerical studies (e.g., Lilly 1962; Pearson 1980). By 12 min (Fig. 14c), the off-axis buoyancy maximum begins to erupt into a secondary thermal via the mechanism of Rayleigh–Taylor instability (Chandrasekahar 1961). The potential temperature gradient along the leading edge of the thermal remains quite sharp, and is typically spread over two computational zones (40 m). The large vortex associated with the descending branch of the primary thermal is well defined and is actively entraining ambient fluid. The buoyancy gradient along the lower portion of the descending branch is also spread over about two computational zones. A second maximum in vertical velocity (8.5 m s^{-1}) occurs at 11 min in the lower center portion of the domain where inertial and buoyancy forces reinforce each other along the upturning branch of the thermal. The wavy appearance of the gradient along the descending branch marks the initial stages of Kelvin–Helmholtz (KH) shearing instability.

By 14 min (Fig. 14e), dramatic changes are evident in the structure of the thermal. The secondary plume near the top of the domain continues to erupt, and the leading edge of the entraining parent vortex remains well defined and coherent after having completed one and one-half revolutions. A series of KH eddies, induced by large velocity and buoyancy gradients, are evident along the descending branch of the thermal (Fig. 14d) and continue to grow throughout the experiment. The maximum downdraft occurs at this time (−13.4 m s^{-1}; Fig. 14d) and has a magnitude greater than the maximum updraft (9.7 m s^{-1}; Fig. 15). The perturbation pressure field (not shown) is characterized by large deficits at the center of each identifiable vortex, the most intense exhibiting a pressure drop of 80 Pa.

In order to verify that the shearing instabilities along the lateral interface of the thermal are indeed of the Kelvin–Helmholtz type, we estimate the ratio of the vertical wavelength of the eddies to the thickness of the shear layer. For a shear layer in which the density and velocity vary linearly, Miles and Howard (1964) used linear theory to show that the wavelength of the fastest growing perturbation is approximately 7.6 times the thickness of the shear layer. In the present case, the density and velocity exhibit an approximately linear structure locally, and we estimate the billow wavelength to be 400 m and the shear layer to be four computational zones wide (80 m). This yields a ratio of 5, which agrees qualitatively with the linear theory. In addition, the Richardson number of the shear layer is approximately 0.10, which is well below the necessary value of 0.25 for instability.

We should note that the size and rate of development of the secondary thermal are sensitive to both the type of rigid boundary condition employed at the symmetry axis (section 3d) and to the spatial resolution (see below). More specifically, "unstaggered" boundaries and low resolution are associated with larger secondary thermals. We therefore cannot be certain that PPM's representation of the secondary thermal is entirely correct, although we do note that this feature is physically

TABLE 1. List of thermal simulation experiments.

Experiment	Grid spacing (m)	Computational domain size	Number of grid zones	Comment
PPM-20S	20	4 km high × 1.6 km wide	201 × 81	
PPM-40S	40	4 km high × 1.6 km wide	101 × 41	
PPM-80S	80	4 km high × 1.6 km wide	51 × 21	
PPM(PL)-40S	40	4 km high × 1.6 km wide	101 × 41	Piecewise linear
PPM(PC)-40S	40	4 km high × 1.6 km wide	101 × 41	Piecewise constant
DW-20S	20	4 km high × 1.6 km wide	200 × 80	
DW-40S	40	4 km high × 1.6 km wide	100 × 40	Discussed only in section 5
PPM-40L	40	8 km high × 3.2 km wide	201 × 81	

plausible and has been reported in other studies of convective elements [e.g., Klassen and Clark's (1985) center-concave clouds].

It is important to note that models formulated using the directional-splitting technique are susceptible to slowly growing instabilities resulting from a spurious generation of vorticity (e.g., Petschek and Libersky 1975; Smolarkiewicz 1982). The origin of this instability lies in the representation of a truly two-dimensional flow by successive one-dimensional calculations. Thus, the structure of a wave propagating obliquely to the grid will, in a directionally split model, be approximated as a series of orthogonal stairsteps rather than a straight line with the length of the stairsteps proportional to the time step. We believe that our model is unaffected by this problem for the following reasons.

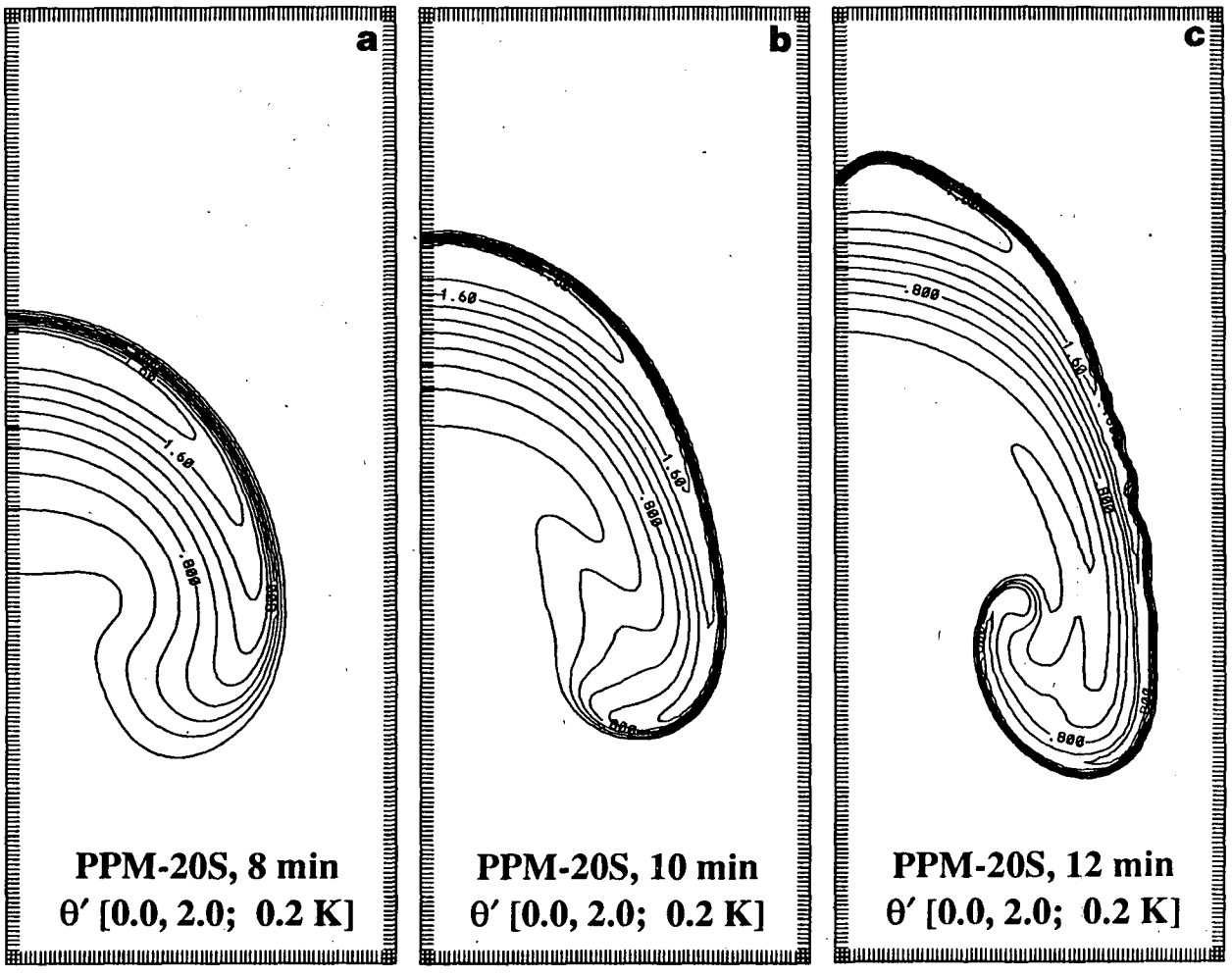

FIG. 14. Perturbation potential temperature (θ', deg K) and vertical velocity (w, m s^{-1}) fields for the control experiment (PPM-20S): (a) θ', 8 min; (b) θ', 10 min; (c) θ', 12 min; (d) w, 14 min; (e) θ', 14 min; (b) θ', 16 min.

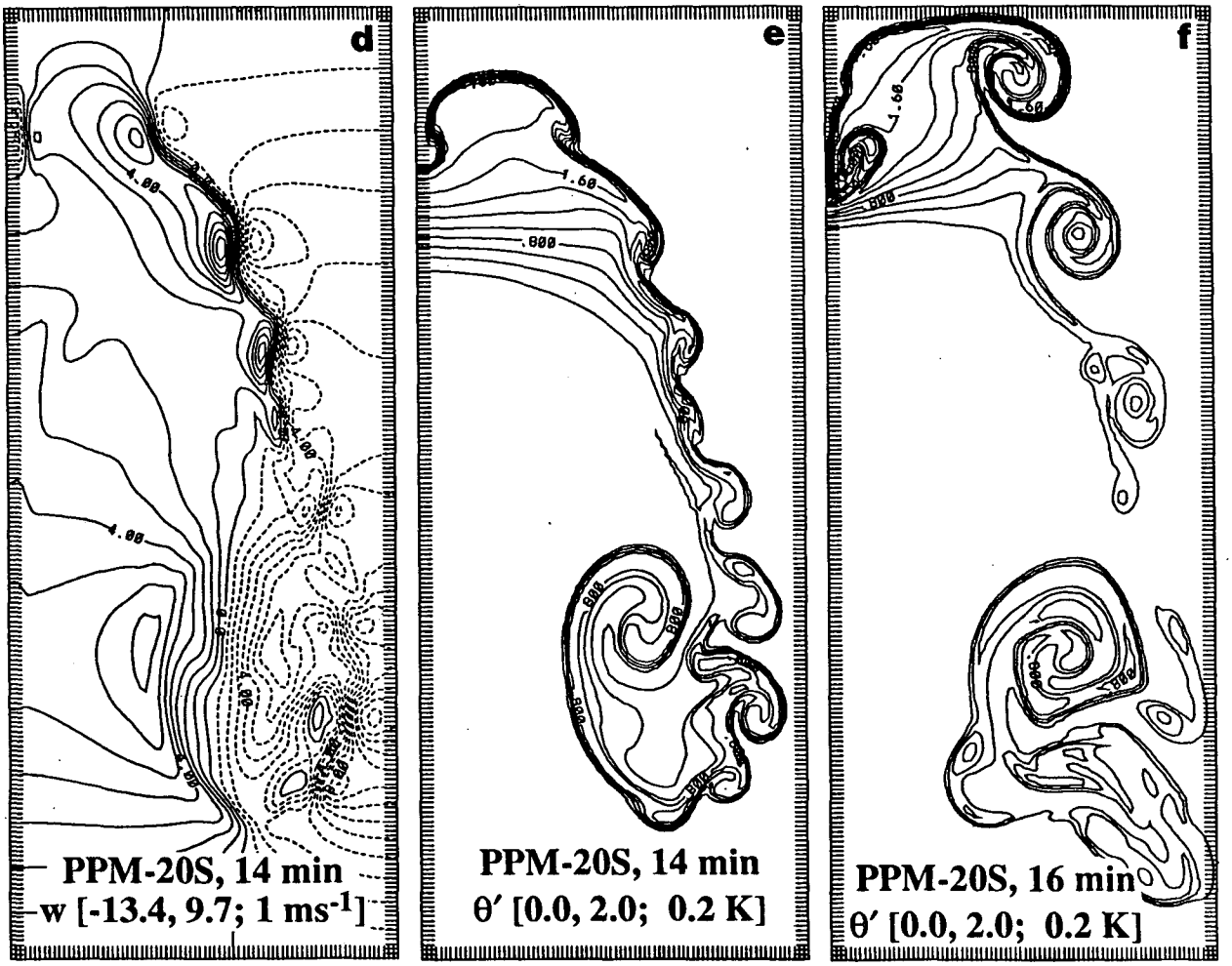

FIG. 14. (*Continued*)

First, implicit models are more susceptible to this instability because the time steps (and thus the directional steps) are larger than in an explicit model (recall that PPM is an *explicit* method). Second, the 2-D advection experiments (section 2b) exhibit no tendency toward stairstepping, and although simulations in this section do show some evidence of this effect (e.g., Fig. 14e), no instability results. Finally, because PPM is a monotonic method, it will never generate spurious maxima in buoyancy. As a result, the associated numerical solutions will exhibit no spurious baroclinic generation of vorticity (see Pearson and O'Connor 1977 for a counterexample).

2) RESOLUTION SENSITIVITY EXPERIMENTS

We now examine the effects of varying spatial resolution on the morphology of the thermal. Reducing the resolution of the control simulation by a factor of two to 40 m (Expt. PPM-40S), we see that at 14 min (Fig. 16a) (when the KH instability in the 20 m run is actively growing)—Fig. 14e), the gross features of the flow agree qualitatively with those of the control experiment. Noticeably absent, however, are many of the smaller scale structures present in the higher res-

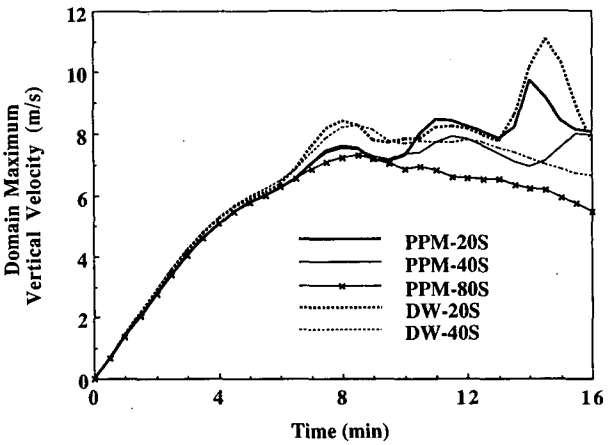

FIG. 15. Time series of domain maximum vertical velocity (m s^{-1}) for the small domain experiments.

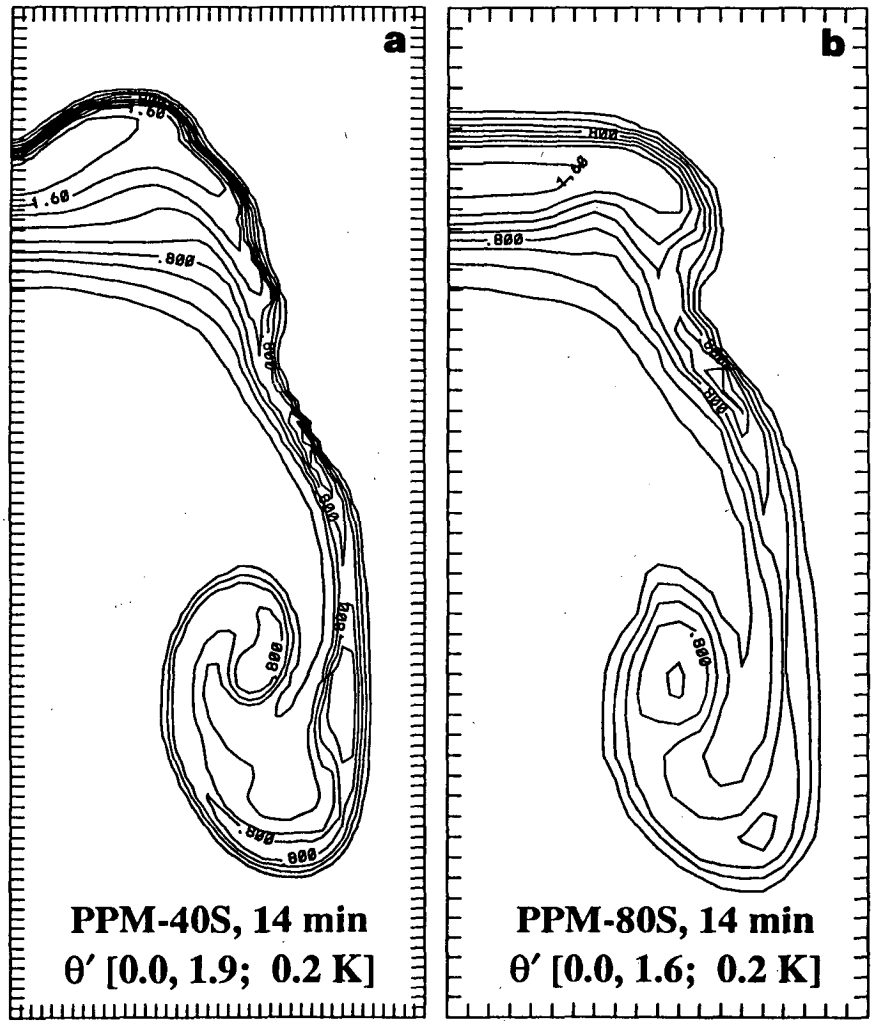

FIG. 16. Perturbation potential temperature (θ', deg K) fields for the variable resolution small domain experiments: (a) PPM-40S, 14 min; (b) PPM-80S, 14 min.

olution experiment. More specifically, the location of the secondary (off-axis) thermal is similar to that in the 20 m experiment, although the former is broader and contains no secondary vortices. The closest agreement between the two simulations occurs in the lower portion of the domain, where the descending vortex entrains a substantial amount of ambient fluid. Note that, despite the use of decreased resolution in the 40 m run (compare Figs. 16a and 14e), most gradients are still spread over no more than two computational zones.

A further decrease in resolution to 80 m (Expt. PPM-80S, Fig. 16b) yields a solution grossly similar to that in the previous experiments, although the secondary (off-axis) buoyancy maximum is not as well defined, and hence no secondary thermal erupts. In addition, gradients along the descending branch of the thermal, though resolved quite well by the code (2 to 4 zone widths), never steepen enough to provide for the onset of KH instability. Despite these differences, the descending branch of the thermal and its associated vortex are similar in overall appearance to those in the higher resolution experiments.

These variable resolution simulations indicate that the bulk features of the buoyant thermal are represented quite well by PPM even at relatively coarse resolution; however, only at sufficiently high resolution is the model able to capture the explicit eddy structures which lead to fully developed turbulence.

3) INTERPOLATION SENSITIVITY EXPERIMENTS

As described in section 2a, PPM represents an extension of lower-order finite volume schemes based on piecewise constant and piecewise linear representations for the dependent variables. In order to assess the additional accuracy afforded by the use of parabolas, we now compare the PPM thermal simulation results with

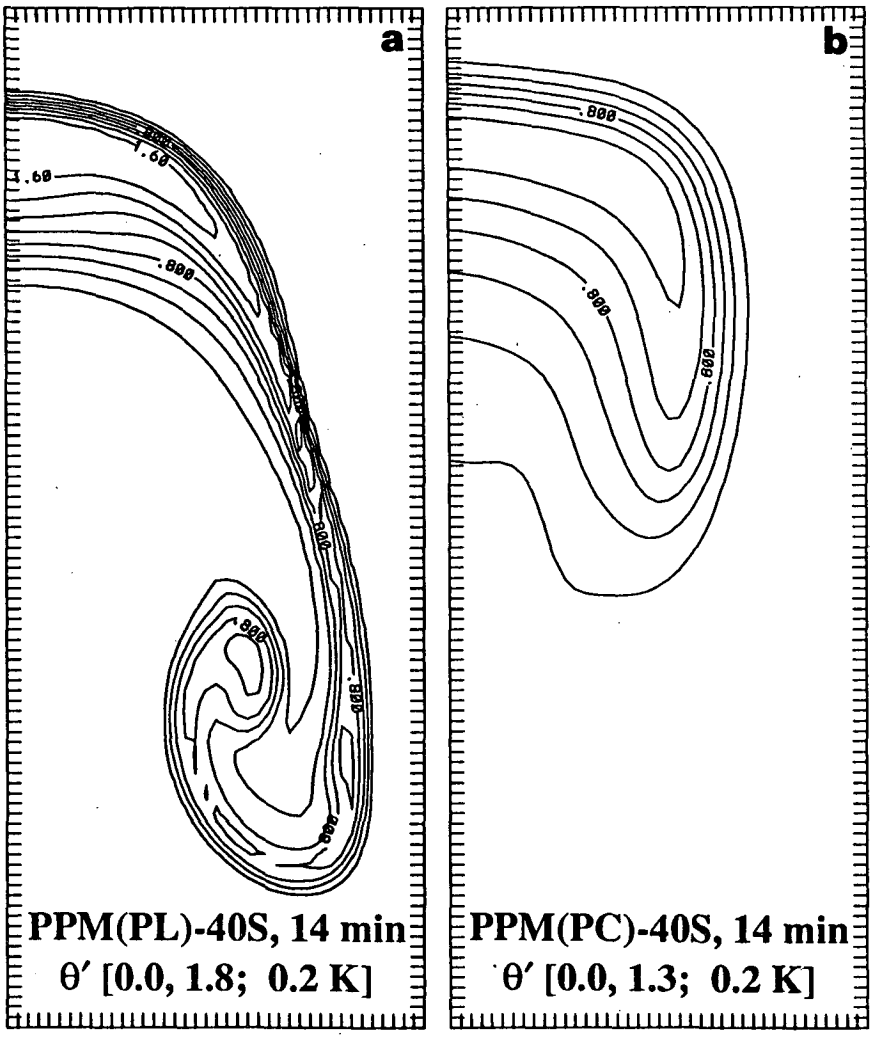

FIG. 17. As in Fig. 16, except for variable interpolation experiments: (a) PPM(PL)-40S, 14 min; (b) PPM(PC)-40S, 14 min.

those produced using piecewise linear and piecewise constant interpolation.

An experiment performed using piecewise linear interpolation [Expt. PPM(PL)-40S] is shown in Fig. 17a. Comparison of this plot with the piecewise parabolic experiment at equivalent spatial resolution (Expt. PPM-40S, Fig. 16a) indicates that piecewise linear interpolation spreads the sharpest gradients over three, rather than two, zones. The potential temperature maximum never leaves the axis of symmetry, and consequently no secondary thermal erupts. Also absent is the vortex away from the symmetry axis seen in the 80 m PPM experiment (Fig. 16b). Once again we find that the solutions agree most closely in the lower region of the domain, and that the multiple shearing eddies present in the 20 m PPM run are completely absent in the piecewise linear experiment.

The perturbation potential temperature field from an experiment using piecewise constant interpolation [Expt. PPM(PC)-40S; Fig. 17b] is quite dissimilar to all results examined thus far, and is characterized by extremely broad gradients and the complete absence of small-scale structure. This result is of no surprise because a piecewise constant representation is equivalent to the highly diffusive first-order upstream scheme (e.g., van Leer 1977).

4) COMPARISON WITH A 2-D CLOUD MODEL

In order to evaluate PPM's capabilities relative to more conventional gridpoint methods, we now compare the PPM solutions with results obtained from a mode-split version of the two-dimensional cloud model developed by Droegemeier and Wilhelmson (1987) (see also Droegemeier and Davies-Jones 1987). This model solves the fully compressible Euler equations in conservation form on a staggered grid using second-order centered differences in time and space. The grav-

itational–acoustic mode-splitting technique of Klemp and Wilhelmson (1978) is employed to overcome the time step limitation imposed by the presence of acoustic waves, and the performance of the model is further improved by artificially reducing the local sound speed, thereby making the flow effectively supercompressible (see DW and Droegemeier and Davies-Jones 1987). Weak background computational mixing is employed to discourage the growth of spurious nonlinear instabilities, and no subgrid scale turbulence parameterization is employed.

Results at 8 min from a 20 m simulation using the DW model (Expt. DW-20S) are shown in Fig. 18a. The thermal is similar in appearance to that in the corresponding PPM simulation (Fig. 14a). Although the evolution of the thermal is quite similar in both models between 8 and 12 min (compare Figs. 14a–c and 18a–c), the leading-edge gradients in the DW model are clearly more diffuse. By 14 min (Fig. 18e), the thermal's shape differs considerably from that of the PPM simulation (Fig. 14e), and the absence of an off-axis buoyancy maximum prevents an associated thermal plume from erupting. The descending branch of the DW thermal is grossly smooth (although some very small-scale noise is present), and the KH wave train present in the PPM experiment never develops even though the interfacial shears (and thus Richardson numbers) are nearly the same (compare Figs. 18d and 14d). (Note the computational noise generated along the descending branch in the DW experiment.) Gradients in the DW experiment are routinely spread over about five or more computational zones, presumably explaining the absence of small-scale shearing instabilities.

After 16 min in the DW experiment (Fig. 18f), a secondary vortex has finally developed in the upper region of the thermal. Its location agrees well with the corresponding vortex in Expt. PPM-20S (Fig. 14f), although the origin of the two vortices is somewhat different (i.e., the vortex in the PPM experiment is gen-

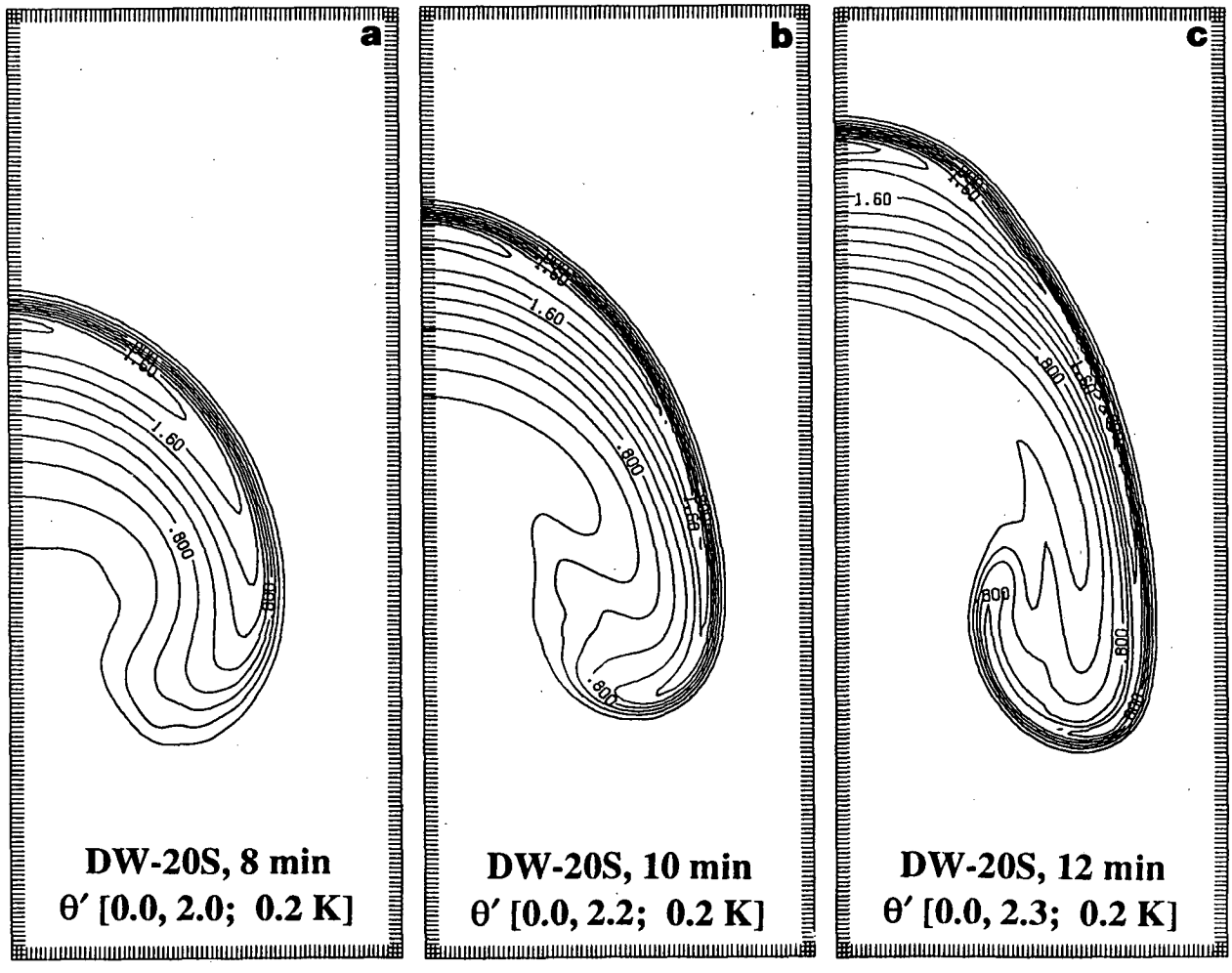

FIG. 18. Perturbation potential temperature (θ', deg K) and vertical velocity (w, m s^{-1}) fields for experiment DW-20S: (a) θ', 8 min; (b) θ', 10 min; (c) θ', 12 min; (d) w, 14 min; (e) θ', 14 min; (f) θ', 16 min.

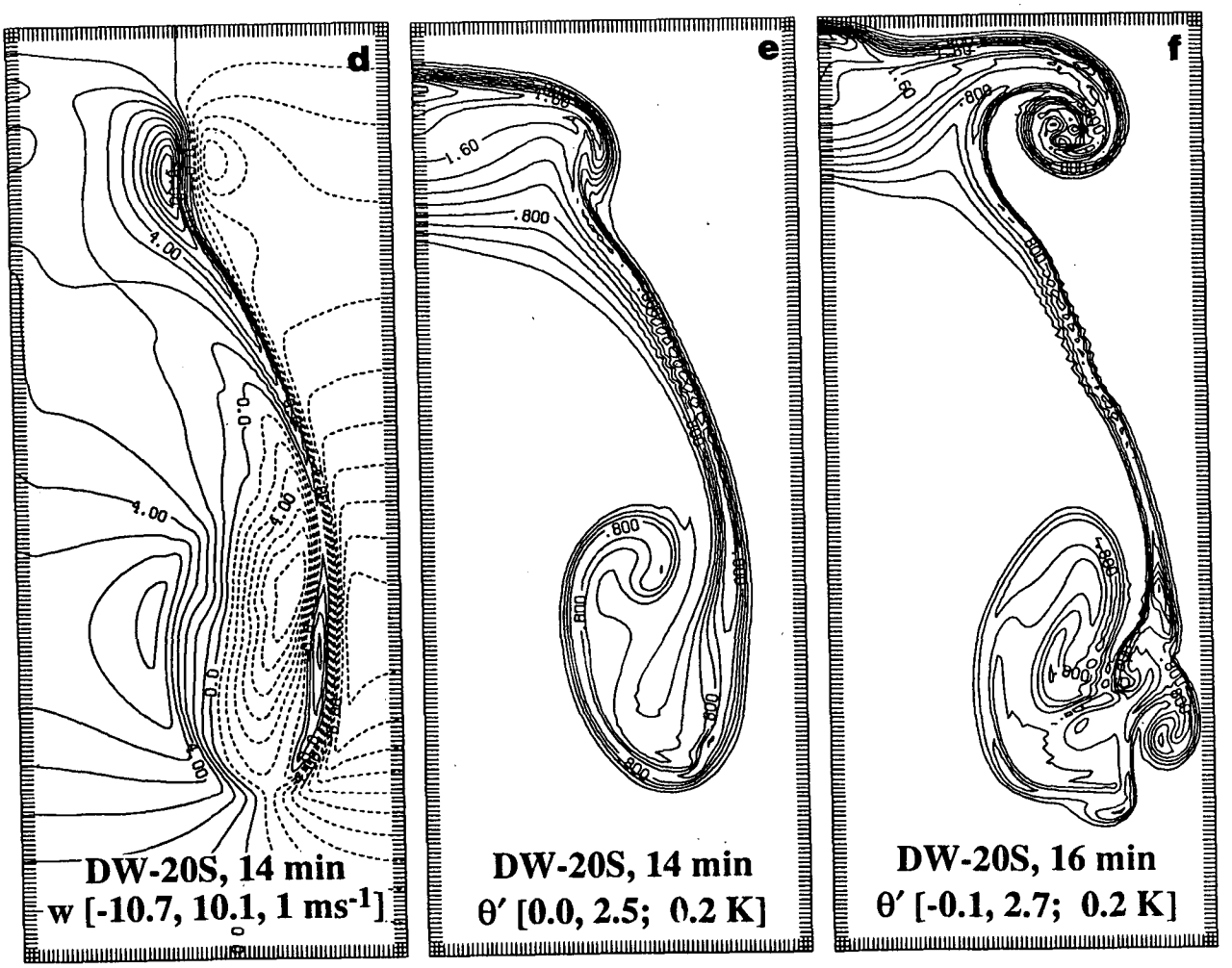

FIG. 18. (*Continued*)

erated by Rayleigh–Taylor instability of an off-axis maximum in the buoyancy, while the DW thermal appears to originate via Kelvin–Helmholtz instability on the side of the thermal). Even though the computational mixing employed in the DW model is of sufficient amplitude to maintain a stable solution, small-scale oscillations (the Gibbs phenomenon) cause the maximum potential temperature perturbation to increase spuriously from its initial value of 2.0 K to 2.7 K by the end of the simulation. In contrast, the monotonicity constraint used by PPM prohibits the generation of such an "overshoot." It is interesting that, in contrast to the PPM experiments and to the other investigations cited earlier, the maximum buoyancy in the DW experiment never leaves the axis of symmetry.

In these and other simulations made with the DW model, the results bear a general resemblance to the PPM experiments. The most notable exceptions involve the small-scale shearing instabilities resolved by PPM and the presence of an off-axis secondary thermal. When these features are present, they dominate the overall structure of the thermal and effectively control its morphology. Small changes in the location of any of these eddies can have a profound impact on the detailed turbulent structure of the evolving flow (although the statistics may be largely unaffected). When the turbulent eddies are unresolved, the thermals are all quite similar and appear to be largely independent of the model or the spatial resolution used.

b. Large domain thermal experiment

In the previous set of experiments, the evolution of a buoyant thermal was simulated in a rather small domain to illustrate PPM's ability to maintain the integrity of sharp gradients relative to a more conventional gridpoint technique. Because the results were controlled largely by the close proximity of the thermal to the boundaries, we now discuss the statistical properties of a more physically realistic experiment using a larger domain. The thermal in this simulation (Expt. PPM-40L) has a maximum potential temperature excess of

3 K and is initially centered 1 km above the lower boundary in a domain 8 km tall and 6.4 km wide (201 × 81 zones). The grid spacing is 40 m and "staggered" rigid boundaries are employed. Although such a boundary condition is unrealistic with respect to atmospheric flows, it does provide for important checks on mass and energy constraints. (A more extensive investigation into the dynamical structure of turbulent thermals will be covered in a future article.)

In the 24 min large domain PPM simulation, the domain-integrated mass is conserved to within one part in two billion. This extreme accuracy results from the associated accuracy of the piecewise parabolic interpolation and advection formulations (see section 2), and from the fact that the model is formulated to conserve mass exactly [Eq. (13)].

Figure 19 illustrates the energy conservation properties for the large-domain simulation (total kinetic energy, total potential energy, total internal energy, and the sum of all components or the total energy) expressed as a percentage change with respect to the initial total energy in the domain. (We choose this method of presentation so that all energy terms may be plotted using the same scale.) Total energy is conserved to within four parts in one hundred thousand, *indicating that PPM exhibits virtually no damping of scales containing significant amounts of energy.*

To quantify the physical realism of the PPM solutions, we now briefly compare our results with similarity theory for slab-symmetric thermals in an incompressible fluid. In a set of numerical experiments, Lilly (1962) found that certain quantities approached similarity more uniformly than others, but that all failed to attain a fully self-similar state. One reason cited was that a true energy cascade is probably not possible in two dimensions, and as shown below our results corroborate this observation.

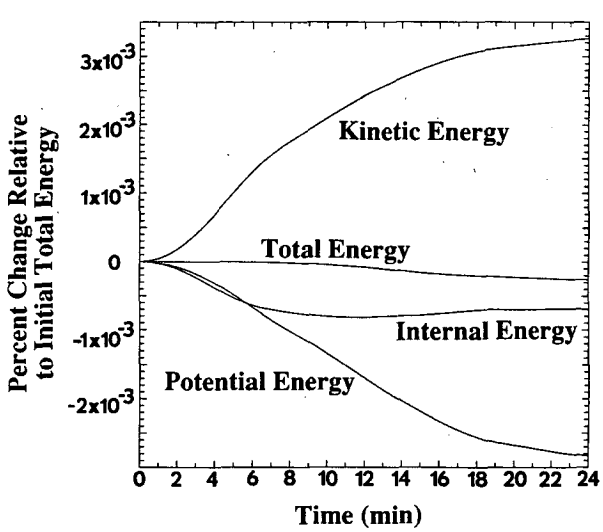

FIG. 19. Time series of the total, internal, potential, and kinetic energy deviations, relative to their initial values and normalized by the initial total energy, for Expt. PPM-40L.

Figures 20a–c show time histories of the total kinetic energy, the maximum perturbation potential temperature (θ'_{max}, deg K), and the maximum vertical velocity (w_{max}) on a log–log scale. Similarity theory states that these quantities should be proportional to time raised to the following powers, respectively: $\frac{2}{3}$, $-\frac{1}{3}$, and $-\frac{4}{3}$. Kinetic energy attains similarity from 7 to 18 min, θ'_{max} after 20 min, and w_{max} after 8 min. Interestingly, three-dimensional models have had little trouble duplicating similarity theory despite the use of resolution that precludes the explicit representation of turbulent eddies (e.g., Fox 1972; Schumann et al. 1987). In a statistical sense this result is not surprising, but simply indicates that the turbulent motions are being represented implicitly by numerical damping and/or by subgrid scale turbulence parameterizations. For problems in which the details of turbulence evolution are important and to a large degree control the flow evolution, e.g., entrainment in convective clouds (Klaassen and Clark 1985), such models would presumably be unable to provide realistic solutions. Indeed, PPM was designed for such problems.

c. Density current experiments

It is not particularly surprising that the DW and PPM model solutions differ considerably in their representation of the *fine-scale structure* of a highly turbulent event. Indeed, the best one might hope for is some sort of statistical agreement in bulk fluid properties (e.g., turbulence spectra). For this reason, it is appropriate to subject both models to a much less violent yet highly nonlinear phenomenon, the density current (see the review by Simpson 1987). Here we focus on a series of experiments reported by Skamarock and Klemp (1989) (hereafter SK), who used an adaptive version of the cloud model developed by Klemp and Wilhelmson (1978) (see also Skamarock 1989 and Skamarock et al. 1989).

As shown in Fig. 21, the initial condition for this set of experiments consists of a cold pool of air that extends from the surface to a height of 5 km in a domain 10 km high and 40 km wide. The potential temperature within the cold pool varies linearly from 290 K at the surface to 300 K at 5 km. In the SK model, the top and bottom boundaries are rigid, frictionless plates, the left boundary is a symmetry condition, and the right boundary employs the radiation condition used by Klemp and Wilhelmson (1978). In the PPM model, "staggered" rigid and frictionless boundaries are employed at the top and bottom of the domain, with a symmetry condition enforced at the left lateral boundary and a radiation condition at the right (see section 3d). The PPM computational domain is also 10 km (41 zones) high and 40 km (160) zones wide, with a uniform grid spacing of 250 m. Experiments using 250

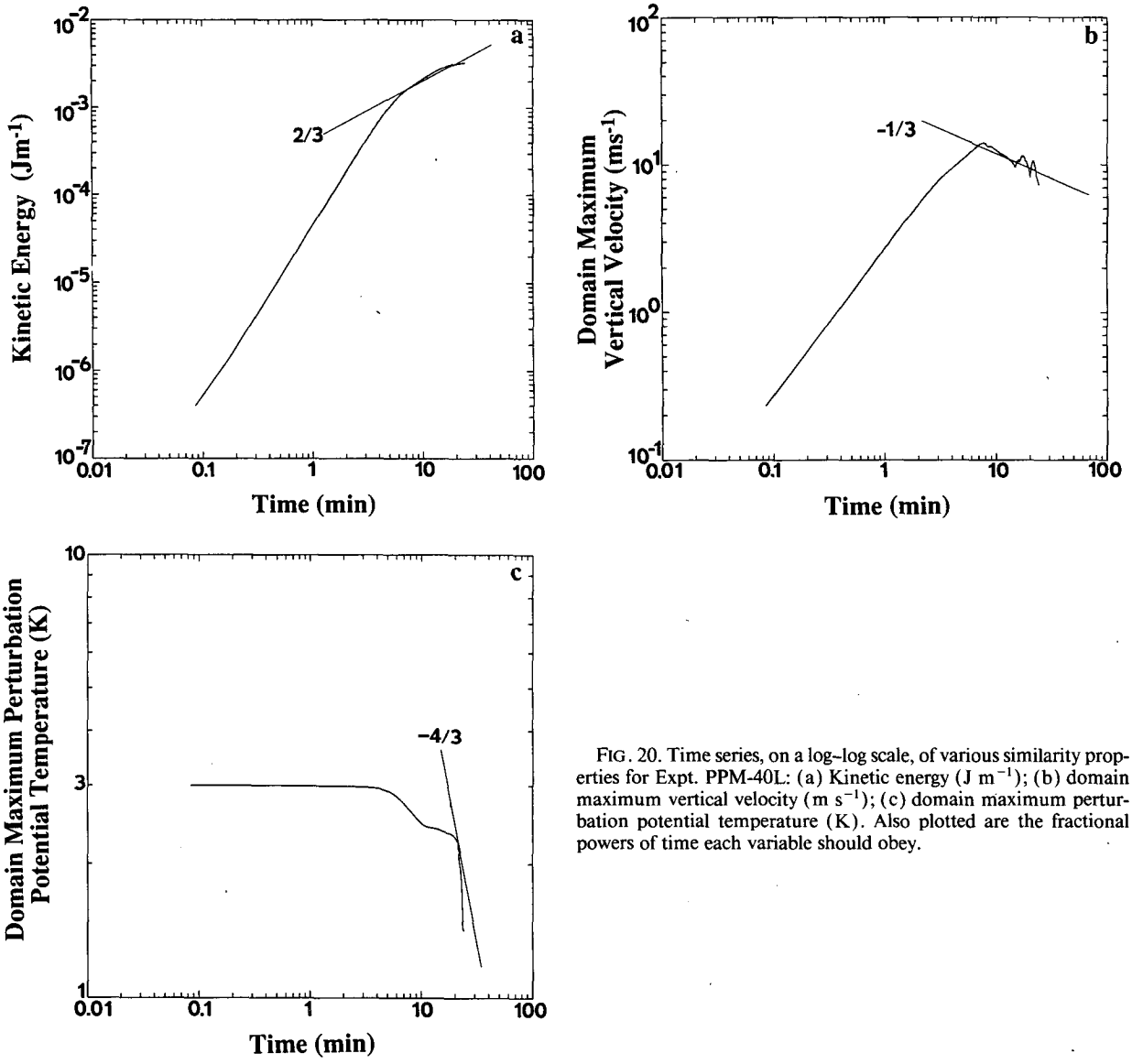

FIG. 20. Time series, on a log–log scale, of various similarity properties for Expt. PPM-40L: (a) Kinetic energy (J m^{-1}); (b) domain maximum vertical velocity (m s^{-1}); (c) domain maximum perturbation potential temperature (K). Also plotted are the fractional powers of time each variable should obey.

m resolution in both models will be referred to as the "coarse-grid" simulations.

The PPM coarse-grid (Δ = 250 m) solution at 900 s is shown in Fig. 22a. A large KH eddy is resolved in the highly turbulent region behind the head of the density current, and the sharp front of the advancing current is well defined and is spread over two zones. On a finer grid (Δ = 83 m, Fig. 22b), several well-resolved eddies are present atop the cold pool and are similar in form to those reported by Droegemeier and Wilhelmson (1987). The coarse-grid (Δ = 250 m) SK solution at 900 s resolves only the bulk features of the flow (i.e., the elevated head region), while the introduction of one level of local grid refinement (Δ = 83 m on the finer grid, Fig. 22d) improves the solution considerably by resolving two eddies within the elevated head region. Employing a second level of grid refinement, so that Δ = 28 m on the finest grid and 83 m on the intermediate grid (Fig. 22e), several more eddies are resolved, including the isolated structure well behind the turbulent wake. Note that this result agrees qualitatively with the 83 m PPM simulation.

On the uniformly coarse grid (Δ = 250 m), PPM clearly resolves more structure than the corresponding SK simulation (compare Figs. 22a and 22c); with one level of refinement in the SK model, the two results are comparable (compare Figs. 22a and 22d), although the SK results appear to be somewhat superior. It is interesting to note that the 83 m resolution PPM solution agrees closely with the highest resolution results of SK (compare Figs. 22b and 22e). In particular, note the similarity in overall eddy structure and the agreement in the slopes of the front and other sharp gradient regions upstream. Although minor stairstepping is ev-

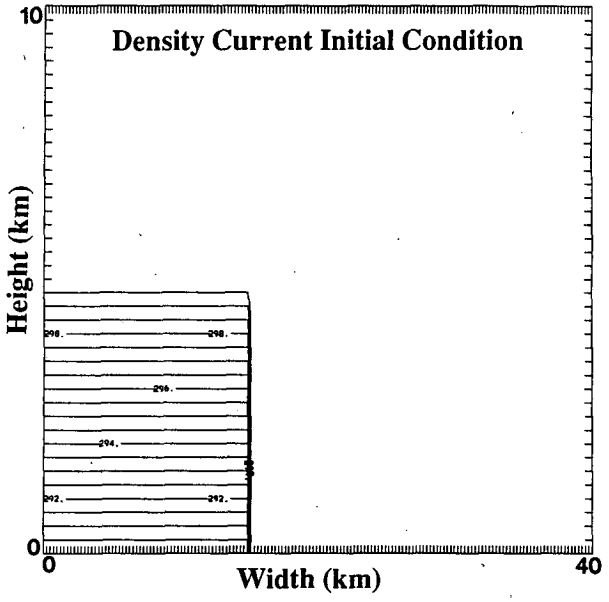

FIG. 21. Initial potential temperature field for the coarse-grid density current simulations. In this and the other density current plots, contours range from 290 K to 300 K with an interval of 0.5 K, except that the 300 K contour has been removed from the PPM simulations.

ident in the 83 m PPM experiment (Fig. 22b), no adverse effects are noted in the solution.

This admittedly limited set of experiments suggests that, for certain physical problems, PPM may be capable of resolving features with ⅓ the spatial resolution required by conventional finite difference schemes. This gain in accuracy must be weighed against computational expense, however, and this issue is addressed in section 5.

5. Evaluation of model efficiency

It is evident from the results examined thus far that, at equivalent spatial resolution on a single grid, PPM provides more accurate results than conventional finite difference methods. To determine if this accuracy is gained without a significant increase in computing cost, we now examine the efficiency by which the PPM, DW, and SK models achieve solutions of *approximately similar* accuracy. We begin by comparing results from the 40 m resolution PPM thermal experiment (Fig. 16a) with those from the 20 m DW simulation (Fig. 18e). Overall the solutions are quite similar in appearance (e.g., the sharpness of the buoyancy gra-

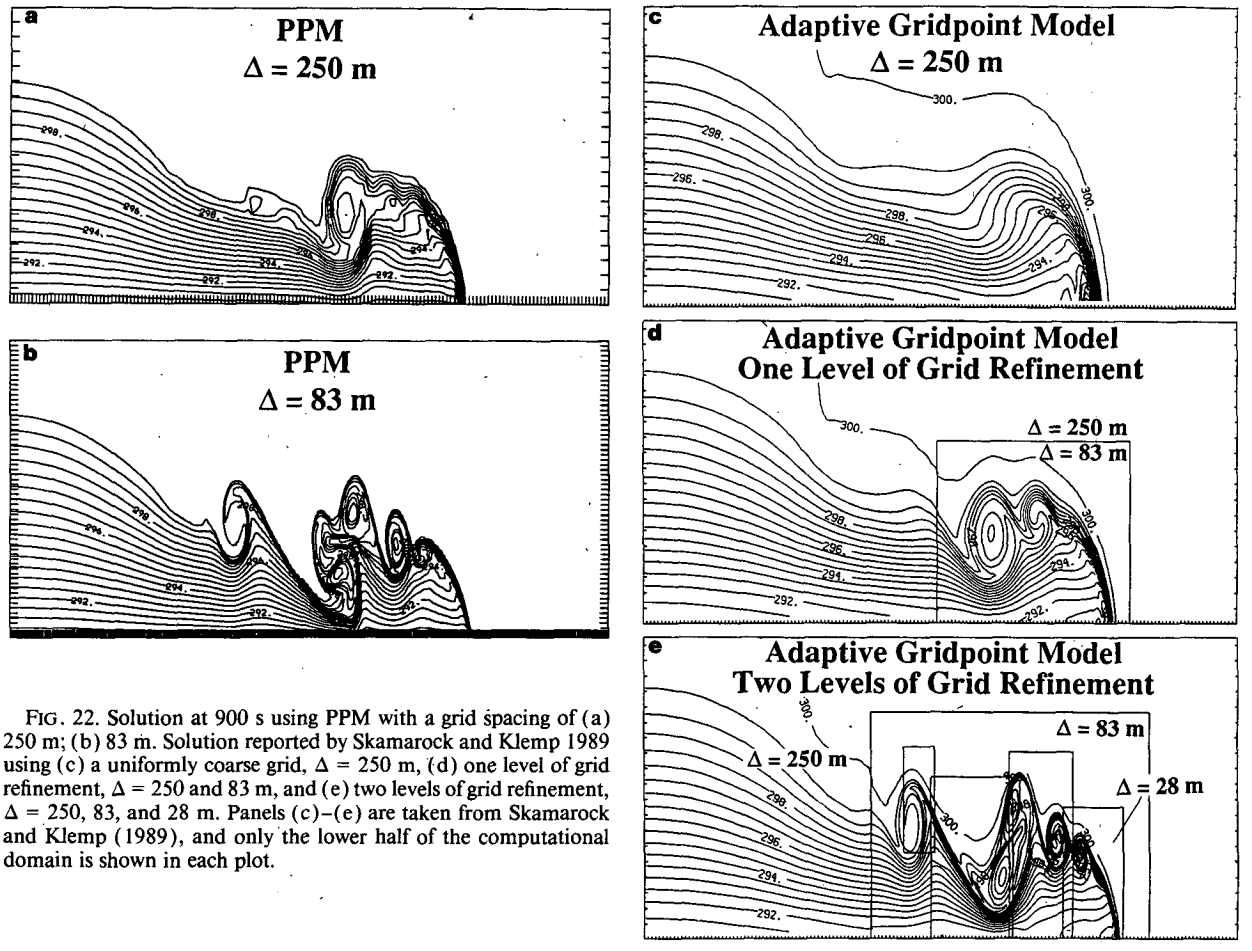

FIG. 22. Solution at 900 s using PPM with a grid spacing of (a) 250 m; (b) 83 m. Solution reported by Skamarock and Klemp 1989 using (c) a uniformly coarse grid, Δ = 250 m, (d) one level of grid refinement, Δ = 250 and 83 m, and (e) two levels of grid refinement, Δ = 250, 83, and 28 m. Panels (c)–(e) are taken from Skamarock and Klemp (1989), and only the lower half of the computational domain is shown in each plot.

dients), *suggesting that PPM yields a qualitatively comparable solution at half the spatial resolution required by the DW model.* (A similar conclusion may be drawn by comparing the 80 m PPM and 40 m DW simulations, and from other experiments not described here.)

Timing statistics for selected small domain simulations are shown in Table 2. Somewhat surprisingly, the 40 m PPM experiment requires only 36% more total central processor unit (CPU) time than its 20 m DW counterpart, even though PPM performs approximately 50% more work per time step. If the cost of the DW simulation is defined as unity, and if we judge PPM solutions at half-resolution to be as accurate as those produced by the DW model, then the relative cost of PPM is 1.36 (i.e., PPM requires 1.36 times as much CPU time as the DW model to produce comparable results).

In evaluating these timing statistics, it is important to recognize that PPM uses a single time step appropriate for acoustic modes while the DW model uses two time steps: a large step for gravitational modes and a smaller step for acoustic modes (the work done in solving the latter is an order of magnitude less than the former, and thus the DW model gains significant speed through the use of this technique). Consequently, a more appropriate assessment of relative CPU performance involves comparing the total CPU time of the 40 m PPM experiment with that of the 40 m DW experiment (figure not shown) in which no mode-splitting and sound speed reduction are employed (Table 2). In this case, the PPM code is approximately 10% *faster* and its solutions superior. Doubling the resolution of the DW model results in solutions comparable to those produced by PPM, but at a factor of 8 increase in cost. This suggests that the cost of PPM is approximately one-tenth that of the DW model for similar solutions using a time step based on acoustic modes alone.

Another measure of PPM's computational cost can be obtained by comparing timing statistics from the 83 m PPM density current simulation (Fig. 22b) with those of the two-level adaptive SK experiment (Fig. 22e) in which a qualitatively similar solution is obtained. Using the CPU times reported by SK, we find that PPM is four times *less* expensive than a single-grid run of the adaptive model (which uses mode-splitting); however, PPM is nearly *twice* as expensive when two levels of adaptive refinement are employed. These results demonstrate not only the economy of PPM *relative to a single-grid simulation,* but also the utility and economy of Skamarock's grid adaption technique.

Recognizing that PPM's inefficiency is based largely on the use of a time step appropriate for meteorologically unimportant acoustic modes, we are working to develop a mode-split version of the code. If, as a conservative estimate, mode-splitting increases PPM's performance by a factor of 5, then based on the comparisons made here, we conclude that PPM may cost only one-third as much as conventional single-grid, finite difference models. Additional savings may be obtained by exploiting the natural parallelism in PPM's directional-splitting formulation.

6. Summary and outlook

We find it quite encouraging that PPM, a numerical *system* designed for accurately depicting sharp gradients in supersonic flows, is apparently well suited for use in modeling small-scale meteorological flows. Even though PPM embodies concepts somewhat foreign to perhaps many meteorological modelers (e.g., the Riemann problem), we find it much more attractive than conventional methods because its rather elegant solution technique is based largely on sound physical principles. Although PPM is, at the moment, somewhat more expensive than conventional gridpoint techniques, the incorporation of mode-splitting should substantially improve its performance, thereby yielding superior solutions at lower spatial resolution and cost.

Using standard linear advection tests, we evaluated the accuracy of the piecewise parabolic interpolation and advection algorithms relative to several conventional finite difference schemes typically used in meteorology. We found that PPM transported functions extremely well when they were well resolved, and that on coarse grids PPM tended to steepen phenomena into square pulses and then transport them faithfully (in contrast to other schemes which distorted and smeared the distributions, often beyond recognition).

TABLE 2. Comparison of model performance for selected small domain thermal simulations.

Experiment	Grid spacing	Time step*	CPU time per grid point per time step*	Total CPU time	Figure
PPM-40S	40 m	0.109 s	14.0	492 s	16a
DW-20S	20	0.400	9.3	361	18e
DW-40S	40	0.800	9.4	46	not shown
DW-40S†	40	0.034	4.8	553	not shown

* For DW, this represents the "large" time step (see text).
† Without time splitting or supercompressibility approximations.

In general, the phase and amplitude characteristics of the PPM solution were superior to all other schemes tested.

Our tests were then extended to two relatively simple yet illustrative nonlinear problems: the evolution of a buoyant convective thermal and a density current in a nonstratified atmosphere. To study these flows, we chose to construct a completely new model rather than use the existing astrophysical version of the PPM code. Our principal modifications included rewriting the governing equations in a form appropriate for atmospheric motion and developing and implementing a simplified solution procedure for the Riemann problem.

Because of its accurate treatment of steep gradients and nearly complete lack of dissipation on energy-containing scales, PPM was quite successful in capturing the turbulent structure of the buoyant thermal and density current, particularly shear-induced instabilities. In the case of the thermal, comparative simulations made with a conventional 2-D cloud model at equivalent resolution were unable to match PPM's accuracy because of excessive numerical diffusion. In the density current simulations, a 2-D adaptive grid-point cloud model produced solutions comparable to those of PPM and at less cost only when the grid was appropriately refined. For single-grid experiments at equivalent resolution, the PPM solutions were superior.

When the PPM interpolation algorithm was replaced by piecewise linear interpolation, some regions of the thermal remained effectively unchanged while others showed little resemblance to the parabolic interpolated solution. This suggests that much of PPM's accuracy would be lost if a lower-order interpolation procedure were used, and that higher-order methods might soon reach a point of diminishing return because of their associated computational expense (a piecewise cubic representation has never been attempted).

Having completed the model development and evaluation phase of our study, we look ahead toward modifying PPM to further enhance its capabilities and performance for meteorological modeling. Many enhancements are currently being investigated, including mode-splitting, the addition of moist microphysical processes, and extension of the model to three dimensions. Because PPM is formulated as a one-dimensional directional split algorithm, the extension to 3-D should be relatively straightforward (a three-dimensional astrophysical version of PPM now exists) and is in fact essential if we hope to simulate turbulence dynamics accurately and recover an inertial subrange. Coupled with its lack of computational damping and accurate treatment of sharp gradients, we conclude that PPM has a tremendous potential for use in meteorological applications.

Availability of videotapes. Animation sequences comparing PPM against other schemes for linear advection, and depicting the time evolution of the simulated thermals, are available in VHS format from the first or second author.

Acknowledgments. The authors benefited from discussions with Douglas Lilly, of the University of Oklahoma, David Porter, of the Minnesota Supercomputer Institute, and Robert Wilhelmson and Louis Wicker, of the University of Illinois. Dr. Andrew Staniforth provided numerous comments which greatly improved the manuscript. Piotr Smolarkiewicz, of the National Center for Atmospheric Research, kindly supplied a copy of his positive-definite algorithm code used in section 2, and brought to light the potential problems associated with directional-splitting techniques. Dr. William Skamarock, of the National Center for Atmospheric Research, kindly supplied us with original figures from his density current simulations, and Ms. Renee Pruett, of the University of Oklahoma, provided helpful comments on early versions of the manuscript. Ms. Sue Weygandt helped prepare the figures, and we are most grateful to Richard Bland, of Cray Research, Inc., for numerous hours of unselfish assistance and for making available the Cray Research Data Center in Mendota Heights, Minnesota.

Equipment used in the research for and preparation of this manuscript was donated by Sun Microsystems, Inc., and by Apple Computer, Inc. The numerical simulations were performed on the Cray-XMP/48, Cray-1A, and Cray X-MP/18 supercomputers at the National Center for Atmospheric Research, which is sponsored by the National Science Foundation (NSF), and on the Cray-2 supercomputer at the Minnesota Supercomputer Institute. Data processing was performed at the University of Oklahoma Geosciences Computing Network. This research represents a portion of the first author's M.S. work at the University of Oklahoma, and was supported by the National Oceanic and Atmospheric Administration under Grant NA85-RAH05046. Additional support was provided by Grants ATM86-57013, ATM86-04402, and ATM88-15371 to the second author from the National Science Foundation, by a grant from the Cray Research Foundation, and by Grants DE-FG02-87ER25035 from the Office of Energy Research and AST86-11404 from the National Science Foundation to the third author at the University of Minnesota.

APPENDIX

Derivation of the Characteristic and Compatibility Equations

Our technique for deriving the characteristic and compatibility equations is standard and can be found in texts on numerical solutions of partial differential equations (e.g., Anderson et al. 1984, 259–272).

The momentum and pressure Eqs. (5) and (6) are augmented with the definitions of the total differentials du and dp':

$$du = \frac{\partial u}{\partial t}\,dt + \frac{\partial u}{\partial m}\,dm \tag{A1}$$

$$dp' = \frac{\partial p'}{\partial t}\,dt + \frac{\partial p'}{\partial m}\,dm. \tag{A2}$$

This system of four equations in four unknowns (the partial derivatives) may be written in matrix form as

$$\begin{pmatrix} 1 & 0 & 0 & 1 \\ 0 & C^2 & 1 & 0 \\ dt & dm & 0 & 0 \\ 0 & 0 & dt & dm \end{pmatrix} \begin{pmatrix} \partial u/\partial t \\ \partial u/\partial m \\ \partial p'/\partial t \\ \partial p'/\partial m \end{pmatrix} = \begin{pmatrix} -\rho' g/\rho \\ \rho_0 g u \\ du \\ dp' \end{pmatrix}. \tag{A3}$$

We proceed as if solving the system using Cramer's rule. By requiring that the determinant of the matrix be zero,

$$\det \begin{bmatrix} 1 & 0 & 0 & 1 \\ 0 & C^2 & 1 & 0 \\ dt & dm & 0 & 0 \\ 0 & 0 & dt & dm \end{bmatrix} = 0, \tag{A4}$$

we may solve for the *differential equations of the characteristics*

$$\frac{dm}{dt} = \pm C, \tag{A5}$$

which are identical to Eqs. (15) in the text.

Next we solve for the *compatibility equations,* which are the original differential equations written along the characteristics. Continuing our solution, we solve for, say, $\partial u/\partial t$ by replacing the first column of the coefficient matrix with the column vector on the right-hand side of (A3) and again setting the determinant equal to zero:

$$\det \begin{bmatrix} -\rho' g/\rho & 0 & 0 & 1 \\ \rho_0 g u & C^2 & 1 & 0 \\ du & dm & 0 & 0 \\ dp' & 0 & dt & dm \end{bmatrix} = 0. \tag{A6}$$

Finally we use the characteristic Eqs. (A5) to obtain

$$d\left(u \pm \frac{p'}{C}\right) = \left(\frac{-\rho' g}{\rho} \pm \frac{\rho_0 g u}{C}\right) dt \tag{A7}$$

which is the continuous analog of Eq. (16) in the text if C is constant.

REFERENCES

Anderson, D. A., J. C. Tannehill and R. H. Pletcher, 1984: *Computational Fluid Mechanics and Heat Transfer.* McGraw-Hill, 599 pp.

Batchelor, G. K., 1954: Heat convection and buoyancy effects in fluids. *Quart. J. Roy. Meteor. Soc.,* **80,** 339–358.

Bennett, A. F., and P. F. Cummins, 1988: Tracking fronts in solutions of the shallow-water equations. *J. Geophys. Res.,* **C93,** 1293–1301.

Boris, J. P., and D. L. Book, 1973: Flux-corrected transport. I: SHASTA, a fluid transport algorithm that works. *J. Comput. Phys.,* **11,** 38–39.

Chandrasekahar, S., 1961: Chapter XI. *Hydrodynamic and Hydromagnetic Instability,* Oxford Press, 481–514.

Colella, P., and P. R. Woodward, 1984: The piecewise parabolic method (PPM) for gas-dynamical simulations. *J. Comput. Phys.,* **54,** 174–201.

Courant, R., and K. O. Friedrichs, 1948: *Supersonic Flow and Shock Waves.* Wiley-Interscience, 464 pp.

Droegemeier, K. K., and R. P. Davies-Jones, 1987: Simulation of thunderstorm microbursts with a supercompressible numerical model. *Proc., 5th Int. Conf. on Numerical Methods in Laminar and Turbulent Flow,* Montreal, 1386–1397. [Sponsored by Concordia University, Pratt and Whitney, Canada, and the National Science and Engineering Research Council of Canada.]

——, and R. B. Wilhelmson, 1987: Numerical simulations of thunderstorm outflow dynamics. Part I: Outflow sensitivity experiments and turbulence dynamics. *J. Atmos. Sci.,* **44,** 1180–1210.

Einfeldt, B., 1988: On Godunov-type methods for gas dynamics. *SIAM J. Numer. Anal.,* **25,** 294–318.

Fox, D. G., 1972: Numerical simulation of three-dimensional, shape-preserving convective elements. *J. Atmos. Sci.,* **29,** 322–341.

Godunov, S. K., 1959: Finite difference methods for numerical computation of discontinuous solutions of the equations of fluid dynamics. *Mat. Sb.,* **4,** 271–306. (*Cornell Aeronautical Lab. Transl.*)

Harten, A., P. D. Lax and B. van Leer, 1983: On upstream differencing and Godunov-type schemes for hyperbolic conservation laws. *SIAM Rev.,* **25,** 35–60.

Holt, M., 1984: *Numerical Methods in Fluid Dynamics.* 2nd ed., Springer-Verlag, 273 pp.

Klaassen, G. P., and T. L. Clark, 1985: Dynamics of the cloud-environment interface and entrainment in small cumuli: Two-dimensional simulations in the absence of ambient shear. *J. Atmos. Sci.,* **42,** 2621–2642.

Klemp, J. B., and R. B. Wilhelmson, 1978: The simulation of three-dimensional convective storm dynamics. *J. Atmos. Sci.,* **35,** 1070–1096.

Lilly, D. K., 1962: On the numerical simulation of buoyant convection. *Tellus,* **14,** 148–172.

——, 1964: Numerical solutions for the shape-preserving two-dimensional thermal convection element. *J. Atmos. Sci.,* **21,** 1070–1096.

——, 1969: Numerical simulation of two-dimensionally isotropic turbulence. *Phys. Fluids Supplement II,* 240–249.

Miles, J. W., and L. N. Howard, 1964: Note on a heterogeneous shear flow. *J. Fluid Mech.,* **20,** 331–336.

Morton, B. R., 1957: Buoyant plumes in a moist atmosphere. *J. Fluid Mech.,* **2,** 127–144.

Noh, W. F., and P. Woodward, 1976: SLIC (Simple Line Interface Calculation). Lawrence Livermore Laboratory Report UCRL-77651, 11 pp. [Available from Lawrence Livermore National Laboratory, University of California, Livermore, CA 94550.]

Norman, M. L., 1980: A numerical study of rotating interstellar clouds: equilibrium and collapse. Ph.D. thesis, University of California and Lawrence Livermore Laboratory, Report UCRT-52946, 223 pp. (see p. 35–41). [Available from Lawrence Livermore National Laboratory, University of California, Livermore, CA 94550.]

Ogura, Y., 1962: Convection of isolated masses of buoyant fluid: A numerical calculation. *J. Atmos. Sci.,* **19,** 492–502.

Parrett, C. A., and M. J. P. Cullen, 1984: Simulation of hydraulic jumps in the presence of rotation and mountains. *Quart. J. Roy. Meteor. Soc.,* **110,** 147–165.

Pearson, R. A., 1980: A discussion on models of thermals. *Pageoph,* **118,** 913–934.

——, and S. O'Connor, 1977: A numerical dynamical instability. *Mon. Wea. Rev.*, **105,** 301–316.

Petschek, A. G., and L. D. Libersky, 1975: Stability, accuracy, and improvement of Crowley advection schemes. *Mon. Wea. Rev.*, **103,** 1104–1109.

Richards, J. M., 1961: Experiments on the penetration of an interface by buoyant thermals. *J. Fluid Mech.*, **11,** 369–384.

Roe, P. L., 1981: Approximate Riemann solvers, parameter vectors, and difference schemes. *J. Comput. Phys.*, **43,** 357–372.

Rood, R. B., 1987: Numerical advection algorithms and their role in atmospheric transport and chemistry models. *Rev. of Geophys.*, **25,** 71–100.

Russell, G. L., and J. A. Lerner, 1981: A new finite-differencing scheme for the tracer transport equation. *J. Atmos. Sci.*, **20,** 1483–1498.

Schneider, H.-R., 1984: A numerical transport scheme which avoids negative mixing ratios. *Mon. Wea. Rev.*, **112,** 1206–1217.

Schumann, U., T. Hauf, H. Holler, H. Schmidt and H. Volkert, 1987: A mesoscale model for the simulation of turbulence, clouds and flow over mountains: Formulation and validation experiments. *Beitr. Phys. Atmos.*, **60,** 413–446.

Scorer, R. S., 1957: Experiments on convection of isolated masses of buoyant fluid. *J. Fluid Mech.*, **13,** 351–368.

——, 1958: *Natural Aerodynamics.* Pergamon Press, 312 pp.

Simpson, J. E., 1987: *Gravity Currents: In the Environment and the Laboratory.* Ellis Horwood, 244 pp.

Skamarock, W. C., 1989: Truncation error estimates for refinement criteria in nested and adaptive models. *Mon. Wea. Rev.*, **117,** 872–886.

——, and J. B. Klemp, 1989: Adaptive models for 2-D and 3-D nonhydrostatic atmospheric flow. *Proc., 6th Int. Conf. on Numerical Methods in Laminar and Turbulent Flow,* Swansea, Wales, UK, 1413–1424. [Sponsored by the Office of Naval Research European Office Engineering Computations.]

——, J. Oliger and R. L. Street, 1989: Adaptive grid refinement for numerical weather prediction. *J. Comput. Phys.*, **80,** 27–60.

Smolarkiewicz, P. K., 1982: The multi-dimensional Crowley advection scheme. *Mon. Wea. Rev.*, **110,** 1968–1983.

——, 1983: A simple positive definite advection scheme with small implicit diffusion. *Mon. Wea. Rev.*, **111,** 479–486.

——, 1984: A fully multidimensional positive definite advection transport algorithm with small implicit diffusion. *J. Comput. Phys.*, **54,** 325–362.

——, and W. Grabowski, 1990: The multidimensional positive definite advection transport algorithm: Nonoscillatory option. *J. Comput. Phys.*, in press.

Squires, P., and J. S. Turner, 1962: An entraining jet model for cumulonimbus updraughts. *Tellus,* **4,** 422–434.

Strang, G., 1968: On the construction and comparison of difference schemes. *SIAM J. Num. Anal.*, **5,** 506–517.

Tennekes, H., 1978: Turbulent flow in two and three dimensions. *Bull. Amer. Meteor. Soc.*, **59,** 22–28.

van Leer, B., 1977: Towards the ultimate conservative difference scheme. IV. A new approach to numerical convection. *J. Comput. Phys.*, **23,** 276–299.

——, 1979: Towards the ultimate conservative difference scheme. V. A second-order sequel to Godunov's method. *J. Comput. Phys.*, **32,** 101–136.

——, and P. R. Woodward, 1979: The MUSCL code for compressible flow: philosophy and results. Proc., Texas Institute of Computational Mathematics Conf., Austin, Texas.

Welch, J. E., F. H. Harlow, J. P. Shannon and B. J. Daly, 1965: The MAC method: A computing technique for solving viscous, incompressible, transient fluid-flow problems involving free surfaces. Los Alamos National Laboratory report LA-3425, 146 pp. [Available from Los Alamos National Laboratory, Los Alamos, NM 87545.]

Woodward, B., 1959: The motion in and around isolated thermals. *Quart. J. Roy. Meteor. Soc.*, **85,** 144–151.

Woodward, P. R., 1986: Piecewise parabolic methods for astrophysical fluid dynamics. *Astrophysical Radiation Hydrodynamics,* K.-H. Winkler and M. L. Norman, Eds., D. Reidel, 245–326. [Also available as Lawrence Livermore National Laboratory Preprint No. UCRL-90009, 83 pp. (1983).]

——, and P. Colella, 1984: The numerical simulation of two-dimensional fluid flow with strong shocks. *J. Comput. Phys.*, **54,** 115–173.

Zalesak, S. T., 1979: Fully multidimensional flux-corrected transport for fluids. *J. Comput. Phys.*, **31,** 335–362.